Predicting the temperature-strain phase diagram of VO_2 from first principles

Chanul Kim

Submitted in partial fulfillment of the
requirements for the degree of
Doctor of Philosophy
in the Graduate School of Arts and Sciences

COLUMBIA UNIVERSITY

2018

ABSTRACT

Predicting the temperature-strain phase diagram of VO_2 from first principles

Chanul Kim

Predicting the temperature-strain phase diagram of VO_2, including the various structural allotropes, from first principles is a grand challenge of materials physics, and even the phase diagram remains unclear at T = 0K. The coexistence of Peierls and Mott physics suggests that a theory which can capture strong electronic correlations will be necessary to compute the total energies. In order to understand the complex nature of the first-order transition of VO_2, we build a minimal model of the structural energetics using the Peirels-Hubbard model and solve it exactly using the Density Matrix Renormalization Group (DMRG) methods demonstrating that the on-site interaction U has a minimal effect on the structural energetics for physical parameters. These results explain the qualitative failures of Density Functional Theory (DFT) and DFT+U for the structural energetics, in addition to the partial success of the unorthodox DFT+U results (i.e. non-spin-polarized and small U). It also guides the creation of empirical corrections to the DFT+U functional which allow us to semi-quantitatively capture the phase stability of the rutile and monoclinic phases as a function of temperature and strain. Our work demonstrates that VO_2 is better described as a Mott assisted Peierls transition.

Contents

List of Figures

List of Tables

Acknowledgements

I would like to express my gratitude to the many people who helped me along this journey. First and foremost, I would like to thank my advisor, Prof. Chris A. Marianetti. His scientific achievements and passion have always inspired me during my doctoral studies. His advice has always been effective and clear whenever I encountered any problems. It has been a great honor for me to work under his supervision.

I would also like to thank all of my colleagues in the Marianetti Group, current and former. Hyowon Park, Hanghui Chen, Pierre Darancet, Yue Chen, Jia Chen, Dalal Kanan, and Alex Taekyung Lee: your knowledge and technical expertise have been invaluable to my research. Eric Isaacs, Xinyuan Ai, Mordechai Kornbluth, Zhengqian Cheng, and Lyuwen Fu: as a fellow student it was very nice having you all as peers to help and support me along the way.

I also would like to acknowledge the assistance of my close friends and classmates: Dennis Wang, Peijie Ong, E-Dean Fung, Timothy Liu, Christopher Choi, and others. During our first years here, we would work together on problems sets and study together for the qualifying and oral exams. During the latter part of my time here, we would offer each other moral support during difficult times. It was very kind of you to help proofread this thesis.

Furthermore, I would like to thank my thesis committee members, Prof. Aron Pinczuk, Prof. Katayun Barmak, Prof. Abhay Pasupathy, and Prof. Nanfang Yu. I am very happy to defend my doctoral thesis under the supervision of the great physicists and materials scientists at Columbia University. Your comments and suggestions have helped strengthen my thesis.

I acknowledge financial support from FAME, one of six centers of STARTnet, a Semiconductor Research Corporation program sponsored by MACRO and DARPA. I would also like to acknowledge the National Energy Research Scientific Computing Center, a DOE Office of Science User Facility for the use of their computing resources as supported by the Office of Science of the U.S. Department of Energy under Contract No. DE-AC02-05CH11231.

Dedication

I dedicate this dissertation to my grandmother, Kwang-soo Lee, and my mother, Mi-sook Jun. Without all the sacrifices they have made for me, I would not be where I am today. It is impossible to thank them adequately for everything they have done. I feel truly grateful to be their grandson and son.

Chapter 1

Introduction

Quantum mechanics is the cornerstone of materials physics that fully describes the motion of and interactions among electrons and atomic nuclei in a solid, and solving the Schrodinger equation is equivalent to revealing all of a solid's structural, electronic, and magnetic properties. However, in reality this is difficult to solve Schrodinger's equations of systems consisting of many interacting bodies due to the associated, often insurmountable, computational costs, which increase exponentially with the number of bodies. Fortunately, with the development of density functional theory (DFT) [1, 2], we can effectively approximate an N-body quantum mechanical equation as N single-body equations by incorporating many-body effects into the so-called exchange correlation potential, significantly reducing the required number of computations. Moreover, the rapid increase of computational power over the years has allowed one to greatly expand the range of materials whose properties can be computed and predicted by density functional theory.

Nevertheless, many interesting materials behaviors still remain elusive because of the limitations of DFT. DFT allows one to in principle solve for the exact ground state observables assuming that the exchange correlation potential is exactly known, but in practice this is never the case. Thus far, the conventional remedy has been to approximate the exchange correlation potential using the local density approximation (LDA) or generalized gradient approximation (GGA), built upon the homogeneous electron gas [2, 3]. The solutions obtained by these approximations are usually at odds with experimental observations of materials with strong electron-electron interactions [4].

These materials are commonly described as strongly correlated. Strongly correlated

materials possess localized orbitals and narrow bands and therefore include many transition metal oxides. VO_2 is one such compound. In addition to having highly localized d-orbitals and narrow bands, VO_2 also belongs to the class of materials containing low-dimensional bands in which the effect of electronic correlations are even more pronounced. This is evident in experimental studies that reported on the one-dimensional nature of the d^1 electronic configuration of VO_2 [5, 6]. Clearly, conventional density functional theory is insufficient to properly describe the materials properties of VO_2 [7], and more advanced techniques such as dynamical mean field theory (DMFT) are needed to capture many-body effects that are ignored in the DFT level of theory.

Many different advanced first-principles methodologies have been applied to VO_2, but only some of them have correctly deduced certain properties [8]. For example, while the calculated electronic structures are accurate, the structural energetics associated with each of its magnetic structures are not. A proper treatment of electron-electron interactions can correct for the inaccurate structural energetics in strongly correlated materials, as evident in a theoretical study carried out by H. Park, A. J. Millis, and C. A. Marianetti [9] describing the phase boundaries in the pressure-temperature plane of the rare earth nickelates. Experimental observations of this phase diagram could not be explained satisfactorily by DFT and the crude but efficient Hartree-Fock solver for DMFT equations (i.e. DFT+U). This can only be fully described when performing the total energy calculations within the combination of DFT and DMFT.

This thesis aims to understand the failure of DFT and DFT+U in describing VO_2, develop a more advanced theory to attain an accurate description of the compound from first principles, and predict the temperature-strain phase diagram of the VO_2 phase transition, which is a grand challenge in materials physics. We first carefully review the first-order phase transition of VO_2, including experimental observations of its allotropes and previous theoretical studies pertaining to the origins of the metal-to-insulator transition accompanying the rutile (R) to monoclinic (M_1) structural phase transition. We then introduce

the Peierls-Hubbard model, which places electron-electron interactions and electron-lattice interactions on equal footing, in Chapter 3. This model is solved through various degrees of approximating the electron-electron interactions. In Chapter 4, we show how the VO_2 phase transition can be interpreted in the context of this model and why only the non-spin-polarized (NSP) solutions from DFT with a small Coulomb interaction U have corroborated with experimental findings in terms of the structural energetics of the transition. Furthermore, we design an empirical functional to describe the phase transition of VO_2 based on physical intuition derived from the Peierls-Hubbard model and previous studies. In Chapter 5, this functional is employed to predict the crystal structure of the R and M_1 phases and the reaction pathway from the former to the latter. We briefly show how the transition temperature of a system can be computed from this first-principles approach. Our empirical functional is then used to compute the phonon spectrum of each phase and, furthermore, predict the temperature-strain phase diagram. Finally, we conclude with a review of the findings in this study and potential future work.

Chapter 2

First-order phase transition of VO_2 and its origins

In 1959, F. Morin discovered that the resistivity of VO_2 changes abruptly by several orders of magnitude at ambient pressure and elevated temperature (i.e. $T_{transition} = 343$ K) [10], which rarely occurs in nature (Figure 2.1.a). Later, it was also proven that the metal-insulator transition can be controlled by other external perturbations electrically [12, 13], optically [14, 15], and through strain triggering [6, 16, 17]. Furthermore, this transition involves a structural deformation with a latent heat of 44 meV/formula units, which manifests as a first-order transition [11, 18]. At high temperatures, VO_2 is a R phase with the space group $P4_2/mnm$ (Figure 2.2.a). This structure consists of a body-centered tetragonal lattice formed by V atoms surrounded by oxygen octahedra. Octahedra linked along the c_R axis share edges, and adjacent octahedra connect with their neighbors at their corners. The Wyckoff positions of the metal atoms are located at (2a): (0,0,0), ($\frac{1}{2}$,$\frac{1}{2}$,$\frac{1}{2}$), while the oxygen atoms are at (4f): ±(u,u,0), ±($\frac{1}{2}$+u,$\frac{1}{2}$-u, $\frac{1}{2}$). An x-ray diffraction study found the lattice constants to be $a_R = 4.5546\mathring{A}$ and $c_R = 2.8514$ $\mathring{A}$ and the internal oxygen parameter u to be 0.301 [19]. The R phase is metallic with Curie-Weiss-like paramagnetism [18, 20]. As the temperature is lowered, there is a first-order transition to a monoclinic (M_1) phase having $P2_1/c$ space group symmetry (Figure 2.2.b). This structure arises from a doubling of the R phase unit cell with accompanying dimerization and antiferroelectric distortion of the V atoms. X-ray methods determine the lattice constants to be $a_{M_1} = 5.743$ $\mathring{A}$, $b_{M_1} = 4.517$ $\mathring{A}$, $c_{M_1} = 5.375$ $\mathring{A}$ and $\beta_{M_1} = 122.646°$, respectively, while the metal atoms and two different types of oxygen atoms occupy (4e): ± (x,y,z), ±(x,$\frac{1}{2}$-y, $\frac{1}{2}$+z) [21, 22]. The M_1 phase is non-magnetic with a temperature-independent magnetic susceptibility and is an insulator

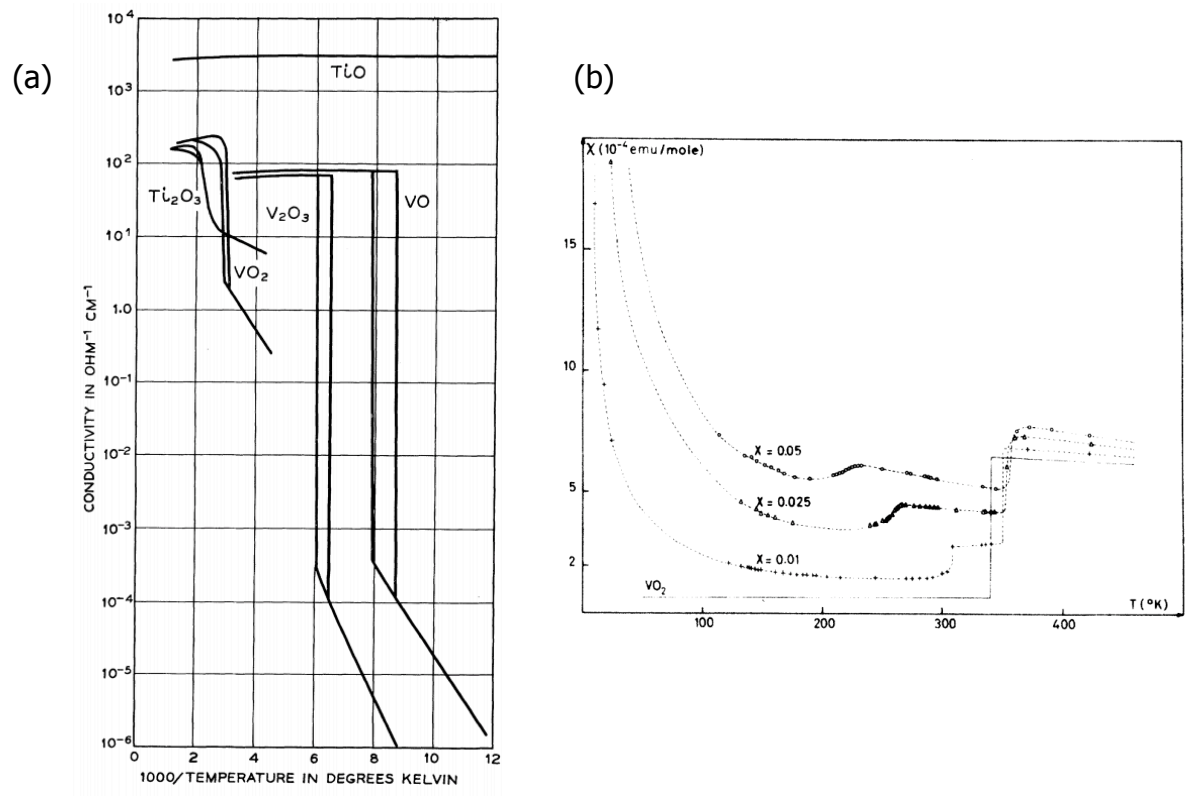

Figure 2.1: (a) Conductivity as a function of reciprocal temperature reproduced from [10]. (b) Magnetic suceptibility of $V_{1-x}Cr_xO_2$ as a function of temperature reproduced from [11].

with an optical band gap of 0.6 eV [23, 24].

This first-order phase transition has drawn much attention arising from possible technological applications over the past 60 years [25–28]. Among its many applications, the most promising is the development of novel, fast, nonvolatile switching devices with ultralow power consumption [12]. The abruptness of the first-order transition allows for fast switching, while the fact that the system enters in a metastable state with only a single electrical pulse gives rise to drastically reduced power consumption. Moreover, these have the potential to overcome issues that currently prevent the further reduction in size of present-day semiconductors, namely the entanglement of electrons below a certain length scale. These unique properties of VO_2 hold great promise for next-generation memory devices. Unfor-

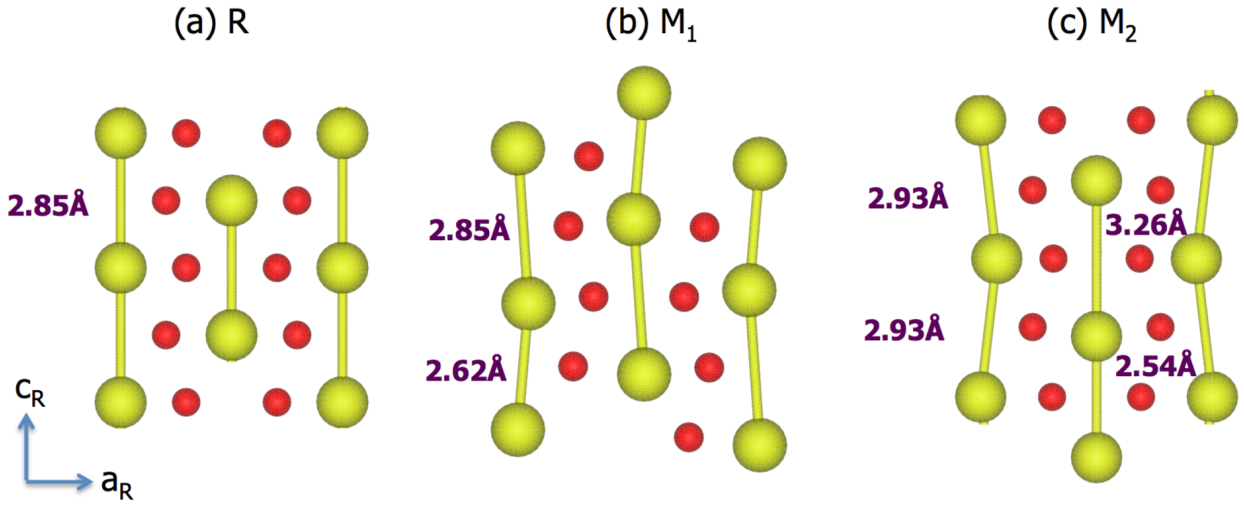

Figure 2.2: A plan view of of crystal structures of (a) R, (b) M_1, and (c) M_2 phase.

tunately, its practical uses are currently limited by a low transition temperature and small band gap. In order to overcome these obstacles, a deep understanding of the complex behavior of the transition is needed and could have far-reaching consequences for industrial applications.

However, the origin of this first-order phase transition was hotly debated for many decades and remains partially unsolved to this day. At the center of the debate was whether the transition was Peierls-like or Mott-like in nature. In the beginning, researchers strongly suspected the former because of the Van-vleck-like paramagnetism and dimerization of V atoms, as indicated by Goodenough in 1971 [29]. The octahedral component of the oxygen crystal field results in threefold t_{2g} and twofold e_g levels; the t_{2g} level is further split into a_{1g} and e_g^{π} levels via orthorhombic distortion. The Peierls distortion (i.e. the doubling of a unit cell) could then occur in the roughly half-filled a_{1g} band, which forms from nearly linear chains along the c-axis, resulting in singlet bonding pairs. Also, the observation of only a modest mass enhancement of electrons in the metallic R phase suggests that strong correlations may not be necessary for the transition [30]. However, an experimental study by Pouget [11] found that another monoclinic structure, known as the M_2 phase (Figure 2.2.c), consisting of two different V-V chains was induced by Cr doping: one was a chain

of dimerized V-V pairs without twisting while the other was a chain of equally spaced V-V pairs with the antiferroelectric shift perpendicular to the rutile c-axis. Nuclear magnetic resonance (NMR) (Figure 2.1.b) and electro paramagnetic resonance (EPR) studies showed that the equally spaced V chain acts like a $S = \frac{1}{2}$ linear Heisenberg chain in the M_2 phase, where the d electrons are substantially localized and developed as local magnetic moments [31]. This observation contradicts the band model. Furthermore, a separate micro-Raman scattering experiment combined with I-V measurements demonstrated that this electric field-driven Mott transition takes place without any structural changes, unlike thermally driven transitions [32]. It is argued therefore that the Mott-Hubbard transition brought about by electron localization is responsible for the electronic gap [33]. While there is evidence of both Peierls and Mott transitions occurring in VO_2, the question remains as to which is more dominant. Numerous experimental observations carried out to this day have not yet determined the precise roles of structural changes (electron-phonon) and electronic correlations (electron-electron), and thus theoretical studies are needed to complete the picture.

All existing first-principles methodologies have been applied to both the R and M_1 phase using their experimentally observed structures over the past several decades [8]. Despite the fact that the experimental structures of these phases utilized by many previous theoretical studies do not necessarily resemble their true ground state, they nevertheless shed some light on the role of crystal deformation and electronic correlations in the phase transition in VO_2. The most basic first-principles approach, DFT, showed that structural distortion alone could not give rise to a proper gap in the experimental M_1 structure, and not surprisingly it also failed to produce a gap in the M_2 phase [7]. This does not necessarily indicate that it is a Mott-type insulator but may imply the important role of electronic correlation in forming a gap. On the other hand, various static Hartree-Fock approaches including DFT+U and a hybrid functional gave a satisfactory gap for the M_1 insulating phases [34–36] but predicted a magnetic ordering inconsistent with experimental observations. GW calculations yielded similar results [37, 38]. The Hedin GW approximation for the single-

electron Green′s function, which is the Hartree-Fock approximation but replaces the bare Coulomb potential by an energy-dependent screened Coulomb interaction, resulted in the insulating M_1 and the metallic R phase [38]. However, it assumed an incorrect magnetic ordering and hence yielded an inaccurate electronic density of states. Among meta-GGAs, the modified Becke-Johnson exchange potential (mBJ) was also used and reproduced the correct electronic structure for the insulating phases [8] but the incorrect ground state for the M_2 phase, which is antiferromagnetic (AFM) according to experiments but nonmagnetic (NM) using this approach[18]. The mBJ potential predicts the NM state to be 160 meV lower in energy than the AFM state. Evidently, the mBJ potential blindly suppresses the formation of magnetic moments, at least in the case of VO_2 [39]. However, it should be noted that the mBJ potential is not meant to be used for total energies because there is no corresponding exchange functional E_x such that $\nu_{x,\sigma}^{MBJ} = \frac{\delta E_x}{\delta \rho_\sigma}$ [40]. The previously discussed theoretical studies suggest, despite their failures, that the inclusion of electronic correlations may be a key ingredient for the gap in the insulating phases of VO_2, but their failures clearly call for a more sophisticated treatment of the electron-electron interaction.

The most promising first-principles techniques beyond Hartree-Fock and DFT are DMFT and its extensions. Single-site DMFT has failed to obtain the insulating phase in the M_1 phase using a reasonable U [41]. Using DMFT with an unphysically large U yields an insulating M_1 phase, a conventional Mott insulator with a local moment and therefore large magnetic susceptibility [43], which are in disagreement with experiment[18]. On the other hand, combining DFT within the LDA with the extended Hubbard model and DMFT (LDA+V+DMFT) captures static intersite correlations, and successfully describes the nonmagnetic insulating phase of the M_1 structure [43]. These calculations indicate that non-local correlations are needed to obtain a proper first-principle description of the VO_2 phase transition.

However, the description of cluster-DMFT varies depending on its implementation. The cluster extension of DMFT, where the oxygen degrees of freedom are eliminated and only

the 3d electrons are considered, has been able to produce a consistent description of both the metallic R phase and the insulating M_1 phase [41]. A robust gap persisting at high electronic temperatures originates from singlet pairs and therefore the non-magnetic state is also captured in the M_1 phase. This is in agreement with experimental observations [18]. The solution obtained in this manner shows a moderate mass renormalization in the R phase and is interpreted as a renormalized Peierls transition. Another cluster DMFT calculation supports this view with an extra analysis to characterize the ground state of insulating phase based on the Hubbard dimer model[46], emphasizing that interstie fluctuations neutralize the on-site Coulomb repulsion. On the other hand, an alternate implementation of cluster DMFT in an ab-initio linear scaling form argued that the gap formation of the M_1 phase mainly comes from an orbital-selective Mott instability involving the a_{1g} electronic states. The recent all-electron embedded cluster-DMFT study [44] supports the Mott-type transition. This calculation found a metallic R phase with strongly renormalized t_{2g} orbitals compared to results from DFT. An insulating gap in the M_1 phase collapses as the electronic temperature is raised, which can only be observed in the Mott state in the presence of strong superexchange coupling (e.g. 2-D Hubbard model [45]). Close to the Mott-Hubbard regime, the strong exchange coupling provides sufficient energy gain to form the strong bonding state of a_{1g}-a_{1g} orbitals. The all-electron cluster DMFT successfully describes the Mott-Hubbard insulating phase, M_2, as well. Given the contradictory results from cluster DMFT calculations, one can see that they suffer from the extremely sensitive physics embedded in VO_2, obfuscating the origins of its phase transition without even incorporating its structural energetics due to the insurmountable computational costs. In this sense, the previous studies have not yet settled the debate.

A clear description of the origins of the phase transition has been largely hindered by the complex physics of the nominal single d electron in VO_2. Specifically, while the extreme cases of dominant kinetic energy and dominant localization energy are straightforward to solve in the Hubbard model, the intermediate regime where VO_2 lies is not as clear-cut [47],

involving multiple interacting degrees of freedom. The behavior of the lone d electrons in this system has been remarkably sensitive to lattice energetics and spectral weight transfer due to changes in the orbital occupations; these may in turn cause dramatic changes in its electronic and magnetic properties. Effectively half-filled a_1g orbtials, induced by a large spectral weight transfer of the VO_2 phase transition, are suceptible to Peierls-distortion causing lattice distortions. Furthermore, Mott-type transitions involve lattice distortions like their Peierl-like counterparts. Examples of these lattice distortions include insulating phases of the rare earth titanates and vanadates stabilized by a $GdFeO_3$-type octahedral rotation [48, 49] and the site-selective Mott transition in nickelates [50]. Based on its sensitivity to minute changes, it is necessary to obtain a full first-principles description of the phase transition of VO_2 in addition to its experimental studies.

In order to decipher these intertwined degrees of freedom, not only should first-principles methodologies be carefully employed and their applicability stringently tested, but the underlying physics of the VO_2 phase transition should also be thoroughly evaluated. Two peculiarities of VO_2 have been overlooked in previous theoretical studies but will be addressed in this thesis. The first is the subtle interplay between the magnetic and structural instability of VO_2. According to recent claims, the electronic properties of both R and M_1 phases can be consistently described using the HSE functional in addition to DFT+U [51, 52]. However, it was recently pointed out that DFT+U and HSE functional yield incorrect ground state solutions for both the R and M_1 phases if spin polarization is allowed, favoring the formation of local moments (i.e. magnetism where there should not be any) and leading to the wrong electronic structure[53]. The same story holds for the recent first-principle quantum Monte Carlo calculations [54]. Furthermore, a spin-polarized solution may kill the dimerization in the M_1 phase since the total energy of the R phase is lower than the that of M_1 phase in that case [39]. Unfortunately, most successful studies done in the past were restricted by the absence of spin polarization and thus fundamentally wrong despite their agreement with experimental observations.

The second peculiarity of first-principles calculation for VO_2 is the lattice energetics predicted by each corresponding functional for first-principles calculations. While it is important to treat the electron-electron interaction with the appropriate field theory, it is equally crucial to identify the correct energetics associated with the lattice reconstruction (which itself depends on the treatment of the electron-electron interaction). Indeed, the structural relaxation within the functional occasionally changes a qualitative feature not captured in the calculation using an experimental crystal structure. In 1994, Wentzcovitch showed that structural relaxation via molecular dynamics calculations correctly yields the M_1 structure, finding the band structure to be slightly gapped. This is in contrast to a complete absence of a gap using the experimental structure of M_1, emphasizing the sensitivity on structural parameters[55]. It is further corroborated by DFT studies employing different lattice parameters that altered the Fermi surface and modified the effective mass of electrons as a consequence of the t_{2g} level shift amounting to a few tenths of an eV [56]. Recent non-spin-polarized DFT+U and hybrid functional studies [52, 57–59] found that the geometrically optimized structure of R and M_1 phases are metallic and insulating, respectively, in reasonable agreement with experiment. However, using the experimental structures, there is no U that opens up a gap in the M_1 phase but closes it in the R phase [60]. Therefore, it is critical to properly account for the full lattice reconstruction in addition to the aforementioned spin polarization when utilizing a first-principles method, in addition to identifying the precise role of the electron-lattice and electron-electron interaction.

Predicting the theoretical crystal structure had been one of the grand challenges in materials physics [61, 62] until sufficiently powerful computers became available to surmount the high computational costs and efficient minimization algorithms were developed to find minima in the complex total energy landscapes of solids. These improvements occured in parallel with advances in implementing density functional theories. Nevertheless, many correlated materials in which LDA and GGA fail to predict the correct crystal structure have been previously documented[63–66]. The most difficult cases to treat are those lying

in the intermediate region between localized and delocalized states. The orbital polarization induced by lattice deformation and Coulomb correlations in VO_2 have equally pronounced effects on its quasiparticle spectra, meaning the electron-phonon interaction and electron-electron interaction are strongly intertwined. Therefore, it is necessary to treat both many-body physics effects, which have thus far caused previous theories to fail, via a more advanced theory and the effect of geometrical reconsturction within its theory to capture the accurate lattice energetics of VO_2 transiton. Only then, can various properties of VO_2 phase be deduced. However, the cost of full structural optimization via advanced theories beyond Hartree-Fock such as DMFT remain unattainably high, forcing users to carry out calculations with experimental structures rather than their true ground state within each corresponding functional. This is the reason why most modern correlated calculations of the electronic properties of both phases are implemented without properly surveying the landscape of the crystal structure via energy minimization and forces to find its equilibrium.

Considering these peculiarities in the previous theoretical studies, only a very limited subset of the unorthodox solutions (e.g. non-spin-polarized and with low interaction energy) have shown promise, and we may need a simplified model of VO_2 to understand why this is so. In the next chapter, we will approximate the phase transition of VO_2 using one of the most simplistic models that places electron-phonon and electron-electron interactions on equal footing to understand the complex interacting degrees of freedom.

Chapter 3

Peierls-Hubbard Model in the context of VO_2

While a full description of any material can be deduced from its corresponding Schrodinger equation, solving it without any approximations remains an impossible task. Even a trusted approximation such as DFT plus cluster DMFT has proven too expensive to perform basic structural relaxations. In this sense, in order to understand the complex phenomena occuring in strongly correlated materials, the first step is to construct a model Hamiltonian that aims to retain the important low-energy degrees of freedom and omit the high energy ones. It would also serve as an inexpensive testbed for the real-material calculations of VO_2 that require prohibitively high computational costs.

While several models for VO_2 have been proposed, model studies of VO_2 from the perspective of energetics are very rare despite its significant importance. The simplest model is that of an isolated single Hubbard dimer at half-filling, which established that the the energy of Heiter-London like wavefunctions is much lower than that of Slater-like wavefunctions if the intra-Coulomb energy is included [67]. This offers an explanation as to why the dimerized phase is nonmagnetic [11, 43, 46]. Another important model for the structural energetics of the transition is a more sophisticated model Hamiltonian consisting of t_{2g} orbitals in VO_2 proposed by D. Paquet and P. Leroux-Hugon [68]. This correctly includes both crystal deformation-dependent moments of the density of states and on-site electron-electron interactions. Nevertheless, electronic correlations were only studied using the functional integral method computed at the (inexact) Hartree-Fock level, resulting in a magnetic moment in the dimerized phase contrary to the exact physical solution in one dimension.

In order to carry out a systematic study, we need a simple but effective model that ap-

proximates the VO_2 phase transition to contain only its most relevant physics. Previous experimental and theoretical studies suggest that the low energy physics of the VO_2 transition is determined by the a_{1g} orbital, which is characterized by one-dimensional hopping. This is largely due to the crystal field splitting arising from hybridization between the vanadium 3d and oxygen 2p orbitals. The crystal fields split d-orbitals into a_{1g}, e_g^π, and e_g^σ[29]. Roughly speaking, e_g^σ and e_g^π are empty and a_{1g} is half-filled since the nominal charge of Vandium is +4, classifying the configuration of Vanadium as d^1. Considering a minimal representation of the correlated subspace to be a_{1g}, we can propose a one dimensional model at half filling that places the electron-phonon and electron-electron interaction on equal footing (Equation 3.1). In this model, the potential energy of the lattice distortion(δ) is taken to be quadratic, accounting for everything not explicitly included in the model (Equation 3.2). The electron-phonon coupling is represented as nearest neighbor hopping parameters that depend linearly upon distance (Equation 3.3). As the atoms in each dimer become closer to each other, their hopping amplitude increases. Conversely, as the atoms in each dimer become more separated, their hopping amplitude weakens. The electron-electron interaction only includes an on-site interaction term as in the conventional Hubbard model (Equation 3.4). The particle-hole symmetry should be observed due to the half filling. This model is in fact the Peierls-Hubbard model, which simply combines the Peierls and Hubbard model (Figure 3.1).

$$\mathbf{H} = \mathbf{H}_{lattice-lattice} + \mathbf{H}_{electron-lattice} + \mathbf{H}_{electron-electron} \tag{3.1}$$

$$\mathbf{H}_{l-l} = \frac{N}{2}\nu\delta^2 \tag{3.2}$$

$$\mathbf{H}_{e-l} = -\Sigma_{l;\sigma}(t - (-1)^l\delta)(c^\dagger_{l,\sigma}c_{l+1,\sigma} + c^\dagger_{l+1,\sigma}c_{l,\sigma}) \tag{3.3}$$

$$\mathbf{H}_{e-e} = U\Sigma_{l=1}^{N} n_{l,\uparrow}n_{l,\downarrow} \tag{3.4}$$

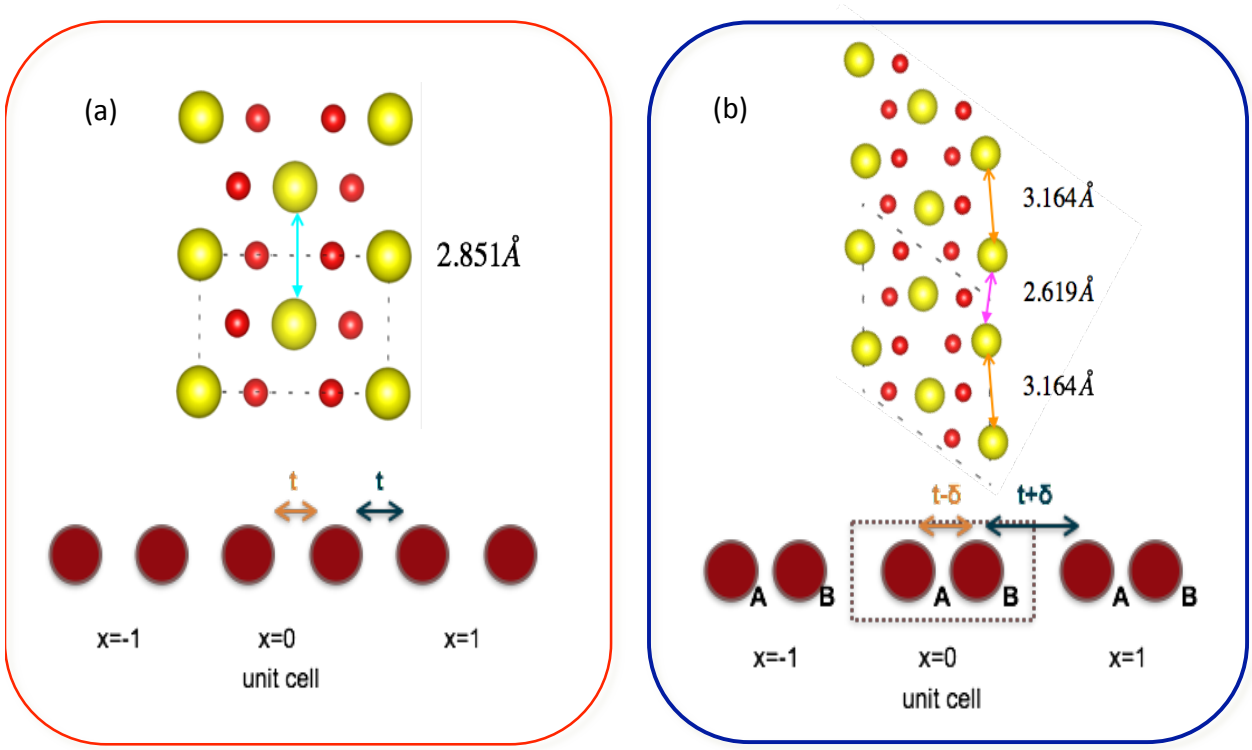

Figure 3.1: Peierls-Hubbard model of the (a) R and (b) M_1 structures.

Solving the two extreme limits of U in the Peierls-Hubbard model is very straightforward. In the non-interacting limit, it is a band insulator due to a Peierls instability. In the strong coupling limit, it is a Mott-Hubbard insulator. However, what lies between the two extremes is much more complex. In the literature, a simple approach via Hartree-Fock [69] and an exact method via the DMRG method [70] differ in their treatment of the electron-electron interaction term, resulting in a striking difference in the calculated total energy as a function of lattice distortion, demonstrating a gross failure of mean field theory. The effect of nesting in the Hartree-Fock treatment in the Peierls-Hubbard model gives rise to a spin density wave rather than a periodic lattice distortion. As a result, the Hartree-Fock solution yields incorrect structural energetics. At the level of Hartree-Fock, including the on-site Coulomb

interaction suppresses the energy gain from the logarithmic singularity and as a result, opposes the structural phase transition [69]. The most advanced treatment of electronic correlations via DMRG, which is exact, results in the true structural energetics in the Peierls-Hubbard model where the dimerization is stablized up to relatively large values of U/t [70]. In order to relate this to approximations used in real materials, it is essential to compute the behavior of the Peierls-Hubbard model using other advanced approximations such as DMFT and its cluster extensions.

In this chapter, we solve the Peierls-Hubbard model energetically with increasingly complex treatments, starting from Hartree-Fock, continuing to DMFT, cluster DMFT, and finally extending it to DMRG. These treatments can be considered as analogous to DFT(+U), DFT+DMFT, DFT+cluster DMFT, and experiments done on the real materials, respectively. Hartree-Fock should capture static correlations and single-site DMFT should capture temporal correlations, whereas cluster DMFT should capture both spatial and temporal correlations. Lastly, DMRG is a numerically exact method in one dimension and will thus capture the exact correlations. This will reveal the effect of the electron-electron interaction on the structural energetics of the Peierls-Hubbard model, and we demonstrate that this will provide the physical intuition needed to interpret previous theoretical studies in a coherent manner.

3.1 Hartree-Fock theory

The most simplistic treatment is the Hartree-Fock method, which views the electron-electron interaction as the lowest order term of perturbataive expansion with respect to the interaction between electrons. It is a static mean field theory that turns the two-particle term into a one-particle term by averaging the contribution from each respective counterpart, as shown explicitly in Equation 3.5. Therefore, this theory inherently neglects all temporal and spatial correlations. These shortcomings prevent Hartree-Fock from explaining one-dimensional

model consisting of correlated electrons.

$$n_\uparrow n_\downarrow \approx n_\uparrow < n_\downarrow > + < n_\uparrow > n_\downarrow - < n_\uparrow >< n_\downarrow > \tag{3.5}$$

Non-spin-polarized case

We first review the non-spin-polarized (NSP) case that restricts spins to be polarized. Here, "non-spin-polarized" indicates that the occupancy of electrons with up and down spins should be equal, written mathematically as $< n_\uparrow >=< n_\downarrow >$. At half filling, the occupancies should be $\frac{1}{2}$, and the electron-electron interaction energy becomes $\frac{U}{4}$. The Fourier transform of the hopping term in the Peierls-Hubbard model is given by Equation 3.6 in units of t, where k-space spans from -$\frac{\pi}{2}$ to $\frac{\pi}{2}$ (lattice vector size is 2).

$$\mathbf{H_k} = \begin{bmatrix} 0 & -1+\delta \\ -1+\delta & 0 \end{bmatrix} + e^{2ki} \begin{bmatrix} 0 & -1-\delta \\ 0 & 0 \end{bmatrix} + e^{-2ki} \begin{bmatrix} 0 & 0 \\ -1-\delta & 0 \end{bmatrix} \tag{3.6}$$

A unitary transformation can be applied to the hopping term, which gives Equation 3.7.

$$\overline{\mathbf{H_k}} = \mathbf{U^\dagger H_k U} = \frac{1}{2} \begin{bmatrix} 1 & 1 \\ 1 & -1 \end{bmatrix} \mathbf{H_k} \begin{bmatrix} 1 & 1 \\ 1 & -1 \end{bmatrix} = \begin{bmatrix} -\alpha(k) & i\gamma(k) \\ -i\gamma(k) & \alpha(k) \end{bmatrix} \tag{3.7}$$

where $\alpha(k) = 2\cos^2 k + 2\delta \sin^2 k$ and $\gamma(k) = (1-\delta)\sin 2k$.

The electron-electron term becomes a one-particle term for the non-interacting case, $\mathbf{H_{e-e}} = \frac{U}{4}$. Since the model is at half-filling, only the lower band is filled. Thus, the total energy is determined by Equation 3.8 consisting of eigenvalues corresponding to the lower band.

$$\frac{E_{tot}}{N} = \frac{\nu}{2}\delta^2 + \frac{U}{4} - \frac{1}{\pi}\int_{-\frac{\pi}{2}}^{\frac{\pi}{2}} \sqrt{\alpha(k)^2 + \gamma(k)^2}dk \tag{3.8}$$

.

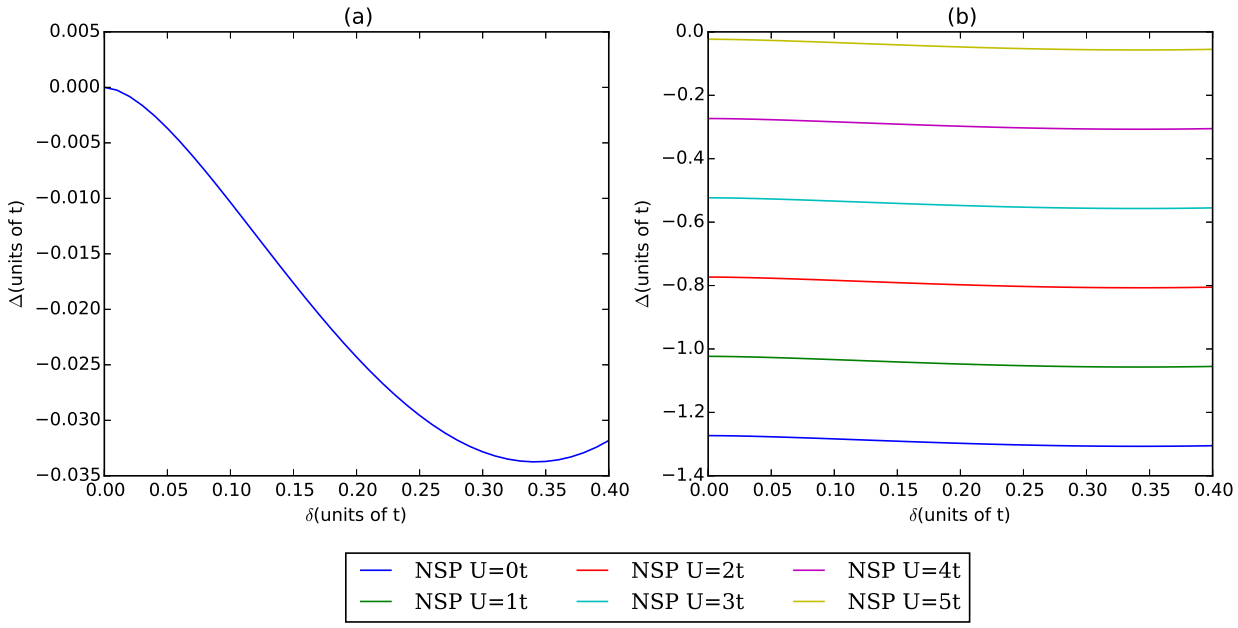

Figure 3.2: (a) Dimerization energy and (b) total energy versus dimerization as a function of U computed by the NSP Hartree-Fock method.

The solutions for the NSP Hartree-Fock Hamiltonian are drawn in Figure 3.2. The dimerization and its energy should remain unchanged regardless of the on-site interaction because the electronic correlation term is independent of δ.

Spin-polarized case

In this subsection, we allow spins to be polarized. The magnetization m_i is defined as $\langle n_{i\uparrow}\rangle - \langle n_{i\downarrow}\rangle$, where $\langle n_{i\uparrow}\rangle + \langle n_{i\downarrow}\rangle$ must equal unity. We consider an antiferromagnetic (AFM) solution because it is lower in energy than a ferromagnetic solution in a one-dimensional system. The spin-polarized condition dictates $\mathbf{H}_{e-e}$ to be $U\Sigma_{l=1}^{N}[\frac{1-m}{2}n_{i\uparrow} + \frac{1+m}{2}n_{i\downarrow} - \frac{1-m^2}{4}]$

The Hamiltonian without the lattice energy should be the following

$$\mathbf{H_{e-l}} + \mathbf{H_{e-e}} = \begin{bmatrix} \frac{U}{4}(1-m)^2 & -(t+\delta) - (t-\delta)e^{2ki} \\ -(t+\delta) - (t-\delta)e^{-2ki} & \frac{U}{4}(1+m)^2 \end{bmatrix} \tag{3.9}$$

in k-space.

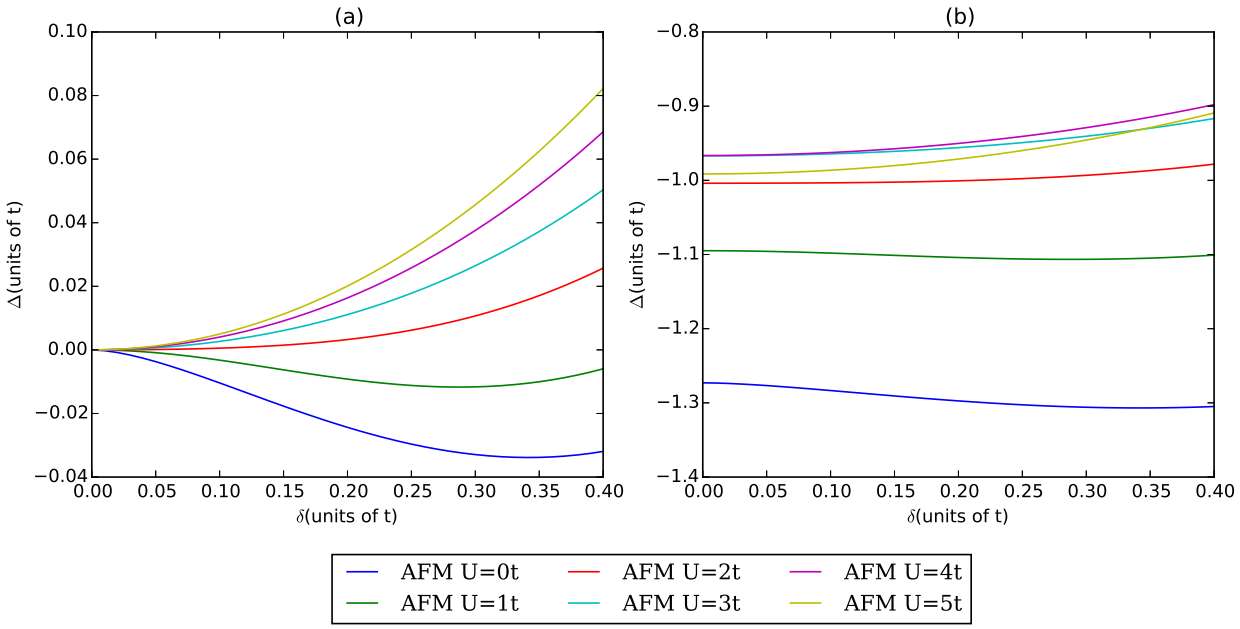

Figure 3.3: (a) Dimerization energy and (b) total energy versus dimerization as a function of U computed by the AFM Hartree-Fock method.

The total energy is derived by minimizing

$$\frac{E_{tot}(m)}{N} = \frac{\nu}{2}\delta^2 + \frac{U(1+m^2)}{4} - \frac{1}{\pi}\int_{-\frac{\pi}{2}}^{\frac{\pi}{2}} \sqrt{4t^2 cos(k)^2 + 4\delta^2 sin(k)^2 + \frac{U^2}{8}(1+m^4)} \qquad (3.10)$$

as a function of m ranging from -1 to 1.

The ground state solutions for the full Hamiltonian are shown as a function of on-site interaction U in Figure 3.3. As the on-site interaction U increases, it kills the dimerization from the electron-phonon interaction and the energy gain associated with the dimerization disappears while lowering the total energy. Therefore, it forms the local magnetic moment without dimerization. This is in agreement with previous first-principles calculations based on static mean field theory.

3.2 Dynamical mean field theory

$$H_{AIM} = H_{atom} + \Sigma_{v,\sigma}\epsilon_v^{bath} n_{v,\sigma}^{bath} + \Sigma_{v,\sigma}(V_v c_{0,\sigma}^{\dagger} a_{v,\sigma}^{bath} + h.c.) \qquad (3.11)$$

In order to bring back the quantum fluctuations of the model, we introduce DMFT that captures the physics of models that stray from the two extremes of tightly bound and itinerant electrons[71]. DMFT is a non-perturbative method that maps the lattice problem to a local quantum impurity problem (Anderson impurity problem) with an effective bath at the cost of losing the momentum-dependence of self energy (Equation 3.11) An impurity having atomic degrees of freedom is modeled as sitting in a bath of electrons with energy levels, $\epsilon_{\upsilon}^{bath}$. The effect of the bath electrons on the impurity is encoded in the hybridization $\Delta(\omega) = \Sigma_{\upsilon}\frac{|V_{\upsilon}|^2}{\omega-\epsilon_{\upsilon}^{bath}}$ which acts a dynamical mean field due to its frequency dependence. The theory properly describes the physics where pure local quantum fluctuations are more highly pronounced than spatial correlation (e.g. infinite coordination number or dimensions). DMFT provides self-consistent relations via the hybridization function (Equation 3.13 - Equation 3.16). The exact local Green's function and self-energy in dynamical mean field theory can be obtained from these self-consistent relations with various impurity solvers.

$$S_{eff} = \int_0^\beta d\tau(\Sigma_\sigma c_\sigma^*(\tau)\frac{\partial}{\partial\tau}c_\sigma(\tau) + H_{at}) + \int_0^\beta d\tau \int_0^\beta d\tau'\Sigma_\sigma c_\sigma^*(\tau)\Delta_\sigma(\tau-\tau')c_\sigma(\tau') \tag{3.12}$$

$$g(\tau-\tau') = -\langle T_\tau c(\tau)c^\dagger(\tau')\rangle_{S_{eff}} \tag{3.13}$$

$$G_(i\omega_n) = \frac{1}{N}\Sigma_k[g^{-1}(i\omega_n) + \Delta_{old}(i\omega_n) - \epsilon_k]^{-1} \tag{3.14}$$

$$\Delta_{new}(i\omega_n) = \Delta_{old}(i\omega_n) + g^{-1}(i\omega_n) - G^{-1}(i\omega_n) \tag{3.15}$$

$$g^{-1}(i\omega_n) = i\omega_n + \mu - \Delta_{new}(i\omega_n) \tag{3.16}$$

While there are many proposed impurity solvers, the iterative perturbation theory approximation (IPT) and continuous-time quantum Monte Carlo (CT-QMC) are notable. In the half-filled Hubbard model, one of the simplest but most efficient solvers of dynamical mean field theory is the iterative perturbation theory that approximates the on-site interaction U term up to the second order Feynman-Dyson diagram constructed with the

Hartree-Fock Greens function. The IPT self-energy can be obtained by Equation 3.18, and a self-consistent solution (G, g_0) is then found by iterating through Equations 3.18, 3.19, 3.20 and 3.21. The resulting solutions describe moderate coupling and also correctly reproduce the extreme limits. This is easily shown by considering the atomic limit $t/U \to 0$, for which $g_0 \approx i\omega_n + \frac{U}{2}$, and the exact Green's function and self-energy are given by $G(i\omega_n) \approx \frac{1}{2}[\frac{1}{i\omega_n+U/2} + \frac{1}{i\omega_n-U/2}]$, $\Sigma(i\omega_n) \approx \frac{U}{2} + \frac{U^2}{4} g_0(i\omega_n)$. Hence, iterative perturbation unifies the weak- and strong-coupling limits, reasonably capturing the Hubbard physics for all U (at half filling). These results are in good agreement with results from CT-QMC and the exact diagonalization impurity solver. Even though IPT is an approximate and interpolative scheme, its computational cost is very cheap due to its analytical form and it works on both the real and imaginary axis at arbitrary temperature. However, it is non-trivial to generalize others models than the half-filled Hubbard model.

$$G(i\omega_n) = g_0(i\omega_n) \tag{3.17}$$

$$\hat{g}^{-1}(i\omega_n) = g_0^{-1}(i\omega_n) - \frac{U}{2} \tag{3.18}$$

$$\Sigma(i\omega_n) = \frac{U}{2} + U^2 \int_0^\beta e^{i\omega_n \tau} \hat{g}_0^2(\tau)\hat{g}_0(-\tau) \tag{3.19}$$

$$G = \int d\epsilon \frac{\rho(\epsilon)}{i\omega_n + \mu - \epsilon - \Sigma(i\omega_n)} \tag{3.20}$$

$$g_0^{-1} = G^{-1} + \Sigma \tag{3.21}$$

The total energy can be obtained from Equation 3.28. The corresponding solutions are plotted in Figure 3.4

On the other hand, CT-QMC is a generalized impurity solver for DMFT that allows for an infinite number of bath levels and gives statistically exact solutions if there is no sign problem that limits its application. The other well-developed methods such as exact diagonalization and the Hirsch-Fye quantum Monte Carlo technique inherit the systematic

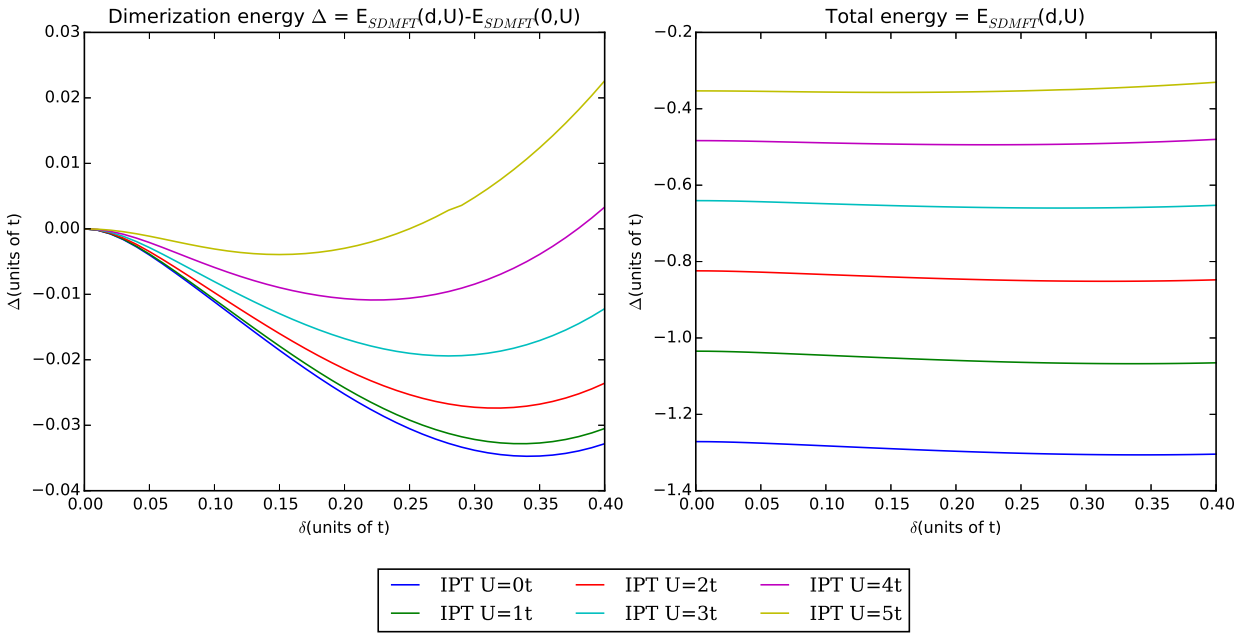

Figure 3.4: (a) Dimerization energy and (b) total energy versus dimerization as a function of U computed by IPT in the single-site DMFT scheme.

errors coming from a discrete representation of the impurity-bath hybridization function for the former or the discretization of the imaginary time interval into slices for the latter. The underlying trick of CT-QMC is to formally expand the partition function as in Equation 3.22 via various implementations such as hybridization expansion without discretizing any physical properties as in Equation 3.23.

$$\begin{aligned} Z = Tr[e^{-\beta(H_0+H_1)}] = Tr[T_\tau e^{-\beta H_0} e^{-\int_0^\beta d\tau H_1(\tau)}] \\ = \Sigma_{k=0}^{\infty} \frac{(-1)^k}{k\,!} \int_0^\beta d\tau_1 \cdots \int_0^\beta d\tau_k Tr[e^{-\beta H_0} H_1(\tau_k) \ldots H_1(\tau_1)] \end{aligned} \tag{3.22}$$

$$\begin{aligned} Z = Tr[T_\tau e^{-\beta H_0} e^{-\int_0^\beta d\tau (H_{hyb}(\tau)+H_{hyb}^\dagger(\tau)} \\ = \Sigma_{k\geq 0} \int_0^\beta d\tau_1 \cdots \int_0^\beta d\tau_{2k} \frac{1}{(2k)\,!} Tr[T_\tau e^{-\beta H_0}((H_{hyb}(\tau_{2k}) + H_{hyb}^\dagger(\tau_{2k})) \ldots (H_{hyb}(\tau_1) + H_{hyb}^\dagger(\tau_1))] \end{aligned} \tag{3.23}$$

Sampling over possible diagrams is done by the Monte Carlo method, resulting in the impurity Green′s function $G_\sigma(i\omega_n)$. The total energy is computed by Equation (3.24) to avoid

noise from the high-frequency behavior of the Green's function, which should be computed analytically rather than from direct sampling.

$$
\begin{aligned}
< H >=< H_{kin} > + < H_{loc} > \\
< H_{kin} >= Tr[\Delta G] + Tr[(\mu + E_{imp})n] = -T < k > + Tr[(\mu + E_{imp})n] \\
< H_{loc} >= \Sigma_{\alpha\beta\gamma\delta} U_{\alpha\beta\gamma\delta} < \psi^{\dagger}_{\alpha}\psi^{\dagger}_{\beta}\psi_{\delta}\psi_{\gamma} > + \Sigma_{\alpha\beta} E_{imp\alpha\beta} < \psi^{\dagger}_{\alpha}\psi_{\beta} >
\end{aligned}
\tag{3.24}
$$

The benefit of CT-QMC is a statistically exact method that is easily generalized to other models (e.g. orbital degeneracy) and works well at various temperatures. However, it is computationally expensive. Lowering the temperature further increases the associated computational cost and causes noise of and sign problem. On the other hand, it works only on the imaginary axis, requiring an analytical continuation approach such as the maximum entropy method to obtain the real-frequency dependent spectra of the Green′s function. Nevertheless, it is not difficult to compute the total energy of a one-dimensional Hubbard model within CT-QMC.

IPT and CT-QMC provide a consistent description of the role of U in the Peierls-Hubbard model, highlighting the fact that the dimerization energy shrinks as U is enhanced, though the rate at which this occurs is slower than that obtained from the AFM Hartree-Fock solution (Figure 3.4 and 3.5) . Note that the CT-QMC solutions are noisy due to convergence issues.

3.3 Cluster extension of dynamical mean field theory

The nature of electronic correlations in one dimension is strikingly different than in three dimensions, as even Fermi liquid schemes break down in one dimension and electron-electron interactions become harder to treat. It has been repeatedly proved that this limit requires much more advanced theory such as the cluster extension of DMFT in order to capture not

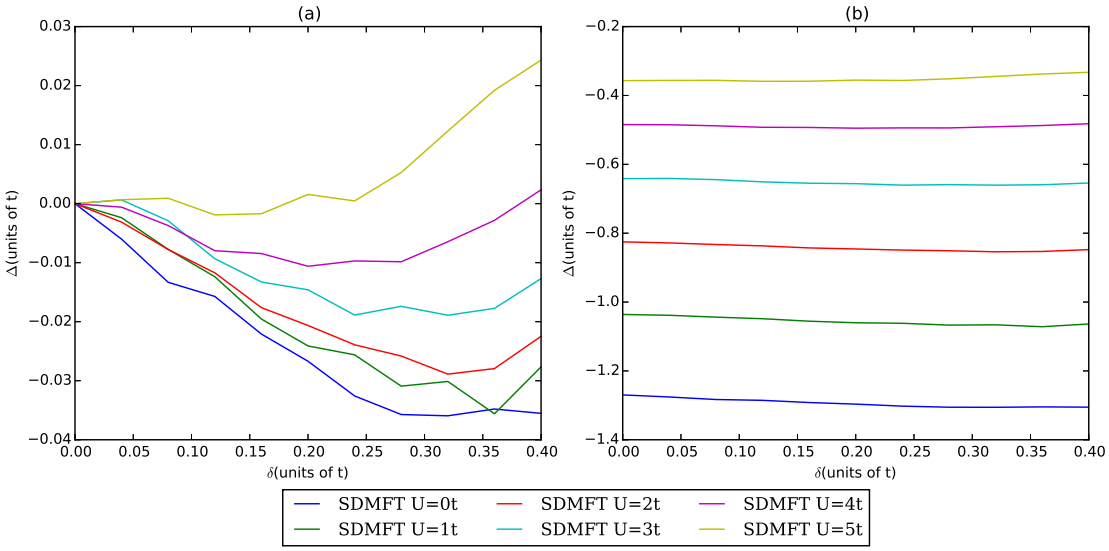

Figure 3.5: (a) Dimerization energy and (b) total energy versus dimerization as a function of U computed by CT-QMC in the single-site DMFT scheme.

only temporal but also spatial correlations [72]. Thus we shall employ the cluster extensions of dynamical mean field theory to solve the one-dimensional Peierls-Hubbard model. While there are several ways to expand a single impurity to a cluster impurity, the most promising ones are cellular extension and the dynamical cluster approximation that systemically determine the spatial range of correlation by the size of cluster with exponentially demanding cost. For example, thermodynamic limit can be attained by using an infinite cluster size (though this is practically infeasible). Cellular DMFT treats an infinite lattice as a series of small clusters [73]. One cluster is chosen while the other clusters act as non-interacting effective bath sites hybridized with it. This yields an approximate lattice self-energy that is finite within the clusters but zero between the clusters. Cellular extension explicitly breaks translational invariance in momentum-space. It performs a real-space coarse graining of the dressed lattice self-energy expansion. Therefore, the momentum and real-space bases are intertwined here. On the other hand, the dynamical cluster approximation performs a k-space coarse graining to map the lattice problem onto a cluster impurity problem with periodic boundary conditions. It needs to interpolate between the value at K_c to restore the

translational invariance in momentum-space [74]. This relation is defined in Equation 3.26, where R_μ is the position vector of μ. Neither of them should violate causality. However, in this subsection, we only perform the total energy calculation of the Peierls-Hubbard model through the simplest case of cellular extension consisting of two-sites clusters since this has been shown to reasonably capture the physics of one dimensional Hubbard model [73, 75].

$$\hat{G}^{loc}(i\omega_n) = \int_{\pi/N_c}^{\pi/N_c} \frac{1}{(i\omega_n + \mu)\hat{I} - \hat{t_k} - \hat{\Sigma}(i\omega_n)} \frac{dk}{2\pi/N_c} \tag{3.25}$$

$$\Sigma(k, i\omega_n) = \frac{1}{N_c} \Sigma_{\mu\nu} e^{ikR_\mu} \Sigma^c_{\mu\nu}(i\omega_n) e^{-ikR_\nu} \tag{3.26}$$

The lattice Green's function of the model is obtained as Equation 3.27

$$\begin{aligned} \mathbf{G}(i\omega_n) &= \frac{1}{2\pi} \int_{-\frac{\pi}{2}}^{\frac{\pi}{2}} (Z\mathbf{I} - \overline{\mathbf{H}}_\mathbf{k})^{-1} dk = \frac{1}{2\pi} \int_{-\frac{\pi}{2}}^{\frac{\pi}{2}} \begin{bmatrix} Z + \alpha(k) & i\gamma(k) \\ -i\gamma(k) & Z - \alpha(k) \end{bmatrix}^{-1} dk \\ &= \frac{1}{2\pi} \int_{-\frac{\pi}{2}}^{\frac{\pi}{2}} \frac{1}{Z^2 - \alpha(k)^2 - \gamma(k)^2} \begin{bmatrix} Z - \alpha(k) & i\gamma(k) \\ -i\gamma(k) & Z + \alpha(k) \end{bmatrix} dk \end{aligned} \tag{3.27}$$

where Z = iω_n + μ - $\Sigma(i\omega_n)$, ω_n is a Matsubara frequency, $\frac{(2n+1)\pi}{\beta}$.

In general, the total energy in the Green′s function approach should be represented as

$$\frac{E_{tot}}{N} = \frac{\nu}{2}\delta^2 + \frac{1}{\beta}\Sigma_n \Sigma_k \frac{2}{N_c} \mathrm{Tr}[(\overline{\mathbf{H}}_\mathbf{k} + \frac{1}{2}\Sigma(i\omega_n)) \cdot [(i\omega_n + \mu)\hat{I} - \Sigma(i\omega_n) - \overline{\mathbf{H}}_\mathbf{k}]^{-1}] \tag{3.28}$$

where N_c is the number of atoms per unit-cell and the associated factor of 2 accounts for spin degeneracy. Furthermore, the corresponding self-energy has been utilized in the bonding-antibonding basis to minimize the computational cost,

$$\overline{\mathbf{\Sigma}}(i\omega_n) = \frac{1}{2}\begin{bmatrix} 1 & 1 \\ 1 & -1 \end{bmatrix} \begin{bmatrix} \Sigma_{00} & \Sigma_{01} \\ \Sigma^*_{01} & \Sigma_{00} \end{bmatrix} \begin{bmatrix} 1 & 1 \\ 1 & -1 \end{bmatrix} = \begin{bmatrix} \Sigma_{00} + \Sigma_{01} & 0 \\ 0 & \Sigma_{00} - \Sigma_{01} \end{bmatrix}. \tag{3.29}$$

The effectiveness of cellular DMFT in capturing the proper energetics of the one-dimensional Hubbard model has been demonstrated at the level of the two-site cluster [76].

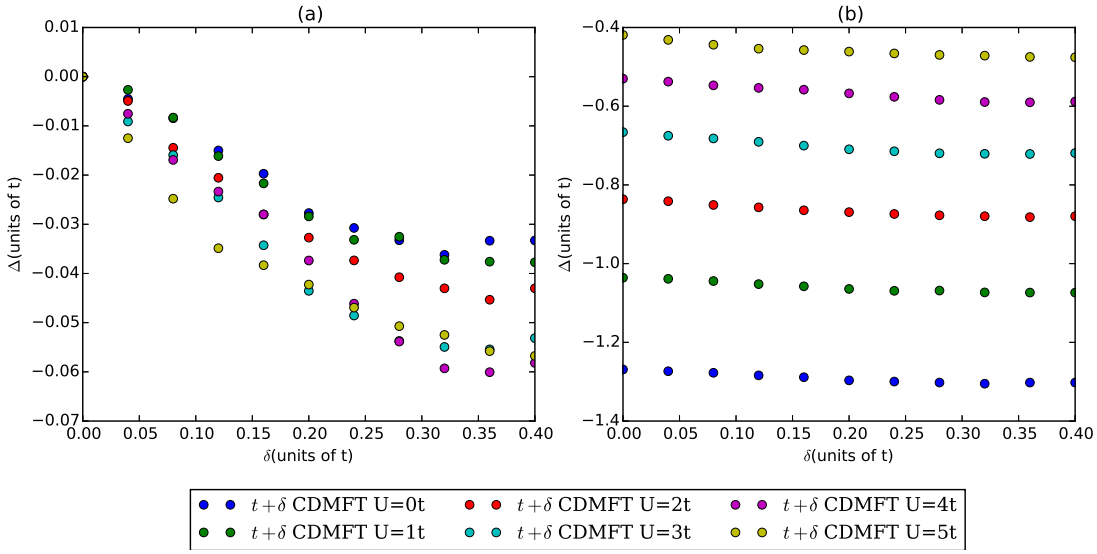

Figure 3.6: (a) Dimerization energy and (b) total energy versus dimerization as a function of U computed by the cellular extension of DMFT using t+δ isolated Hubbard dimer impurity

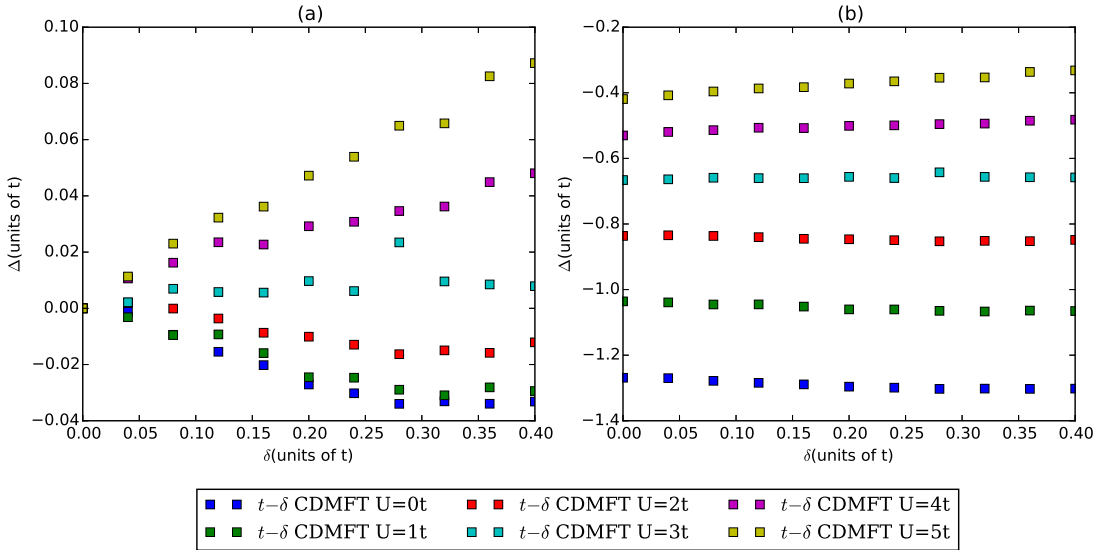

Figure 3.7: (a) Dimerization energy and (b) total energy versus dimerization as a function of U computed by the cellular extension of DMFT using t-δ isolated Hubbard dimer impurity

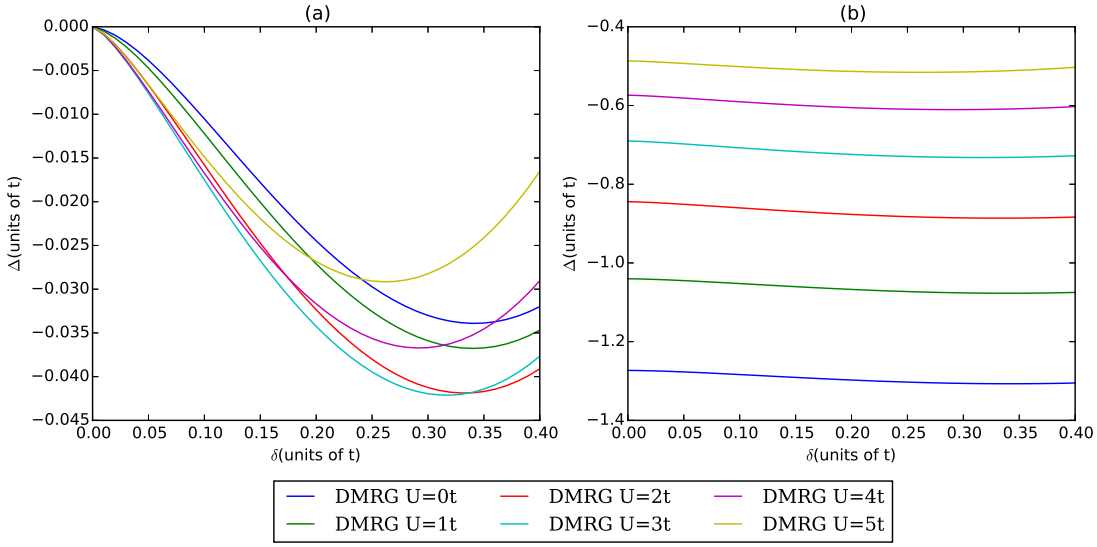

Figure 3.8: (a) Dimerization energy and (b) total energy versus dimerization as a function of U computed by the DMRG method

However, the two-site cluster forces one to choose between t+d and t-d for the intersite hopping parameter. The cellular DMFT of the Peierls-Hubbard model shows that the former overestimates the dimerization energy (Figure 3.6) while the latter underestimates the dimerization energy (Figure 3.7). Unlike the previous solutions from AFM Hartree-Fock and DMFT, CDMFT using t+d clusters shows that the dimerization is enhanced as U is included.

3.4 Density matrix renormalization group

The DMRG method systematically reduces the degrees of freedom of the effective model Hamiltonians, providing an exact solution for intractable systems in one dimension [77]. We utilized the finite-size algorithm implemented in Algorithms and Libraries for Physics Simulations [78, 79]. The accuracy of the model calculation is obtained by using a chain of 100 sites. The total energy is computed by substracting the energy of 100 sites from the that of 102 sites and dividing it by two, $\mathrm{E}_{totphm} = \frac{E_{L=102}-E_{L=100}}{2}$. The energy gap of the Peierls-

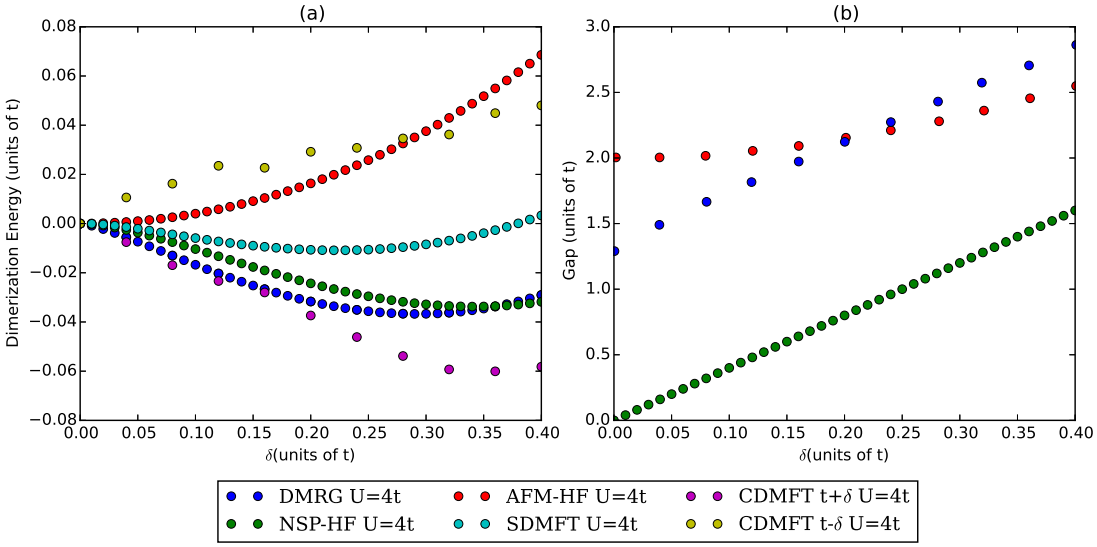

Figure 3.9: (a) Dimerization energy obtained by NSP Hartree-Fock (NSP), antiferromagnetic Hartree-Fock (AFM), density matrix renormalization group (DMRG), single-site dynamical mean field theory (s-DMFT), and cluster dynamical mean field theory (c-DMFT) (b) Gap versus dimerization as computed by NSP Hartree-Fock, AFM Hartree-Fock, and DMRG.

Hubbard model is obtained by the energy difference between the first excited state and the ground state in the thermodynamic limit. The (exact) DMRG solution demonstrates that as U increases up to moderate U, the dimerization is enhanced (Figure 3.8).

3.5 Non-locality of structural energetics in the Peierls-Hubbard model

We have shown that the 1D Peierls-Hubbard model can be solved by different levels of approximations for the correlations. The total energy versus dimerization is drawn from the Peierls-Hubbard model solutions of various approximations using the physical parameters of VO_2, U=4t in Figure 3.9. The exact (DMRG) solution favors dimerization while the Hartree-Fock solution and single-site DMFT suppress dimerization. NSP Hartree-Fock qualitatively captures the exact solution behavior and a two-site cellular extension of DMFT

restores a large portion of the physics by capturing non-local electron-electron correlations. However, both cluster extensions to DMFT will eventually yield exact solutions if they include many sites in the cluster. We have not performed many-site cluster calculations to describe the physics in greater detail because they are likely computationally infeasible for real-materials calculations for VO_2. In this sense, the various levels of approximations clarify the non-locality of the structural energetics even though the model Hamiltonian contains only a local interaction term in addition to a non-local hopping term. While the need for advanced theories beyond Hartree-Fock are emphasized here for real-materials calculations, the most practical approximation is to completely ignore the electron-electron interaction. This inevitably leads one to deliberately design a non-spin-polarized DFT-based approach to successfully describe the VO_2 transition. Note that the NSP Hartree-Fock solution predicts much less a_{1g}-a_{1g} splitting than the (exact) DMRG solution. The interpretation of results from DFT+U will be carried out based on our understanding of the Peierls-Hubbard model, and its implications will be used to extend the DFT+U functional in the next chapter.

Chapter 4

Designing a single-particle matrix density functional for VO_2

In this chapter, we first review the applicability of DFT-based theories to VO_2 from the perspective of structural energetics in the Peierls-Hubbard model. This will shed light on why, within DFT+U, antiferromagnetic solutions kill dimerization and the restricted non-spin-polarized solutions give a reasonable baseline. It should be noted that there is a critical feature of VO_2 that is not accounted for in the Peierls-Hubbard model, which is the presence of other d-orbitals that may decrease the electronic density of the a_{1g} band, greatly altering the low-energy physics. In our DFT-based approach, we introduce two extra parameters, α and β, in addition to the on-site interaction U to obtain the proper orbital filling and configuration.

The density functional theory calculations in this thesis are implemented in Vienna Ab-initio Software Package (VASP), which utilizes a plane-wave basis set and the projector-augmented wave (PAW) method [3, 81–86]. Correlation effects associated with the 3d orbitals are further explored using the DFT+U method [87]. The DFT+U method requires the definition of the on-site Coulomb repulsion U, and we do not include an on-site exchange interaction J given that this is effectively accounted for within the spin-dependent exchange-correlation potential [88]. All results were obtained using a 500 eV plane wave cutoff. A $9 \times 9 \times 15$ Monkhorst-Pack k-point mesh centered at Γ is sampled for both M_1 crystal structures consisting of 4 formula units and R crystal structures consisting of 2 formula units [89]. The total energies of each structure are minimized using the Hellmann-Feyman theorem and conjugate gradient algorithm [90]. The lattice parameters and atomic positions are relaxed until the total energy changes by less than 10^{-5} per unit cell and the residual

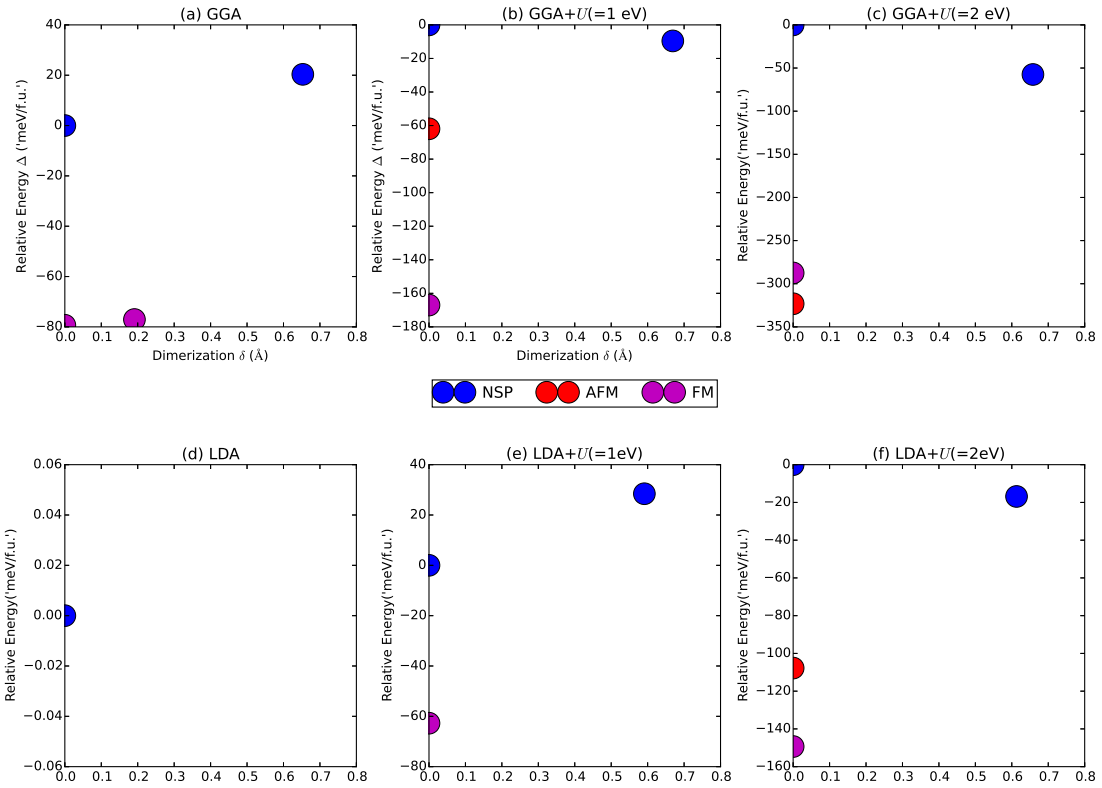

Figure 4.1: Relative energies ΔE with respect to the NSP R phase (meV/formula unit) and dimerization length δ ($\mathring{A}$) are plotted using (a) GGA, (b) GGA+U(= 1eV), (c) GGA+U(= 2eV), (d) LDA, (e) LDA+U(= 1eV), and (f) LDA+U(= 2eV). The absence of data points indicates that the crystal and magnetic structures have relaxed back to other phases, and thus the existence of data points manifest their metastability. The magnetic orderings represent the spins of V atoms along the c-axis.

force is less than 0.01 eV / $\mathring{A}$. The tetrahedron method is used for Brillouin zone integration.

The crystal structures are drawn using VESTA code [91].

4.1 Failures of DFT(+U) in structural energetics of VO_2

In this section, we present the structural phase stability of VO_2 by considering its full magnetic solutions and geometrical relaxation through the LDA, GGA and their Hubbard U corrections in Figure 4.1. The phase stability was examined using the experimental structure, and full relaxations have been considered using NSP DFT and DFT+U, but there has not been a proper study identifying the true ground state of the DFT functional (i.e. possibility of magnetic states) while also performing structural relaxations. We therefore rigorously study the phase stability allowing for all symmetry breaking (i.e. magnetic, orbital, etc.).

First, GGA without U is employed to study the energetics for both the R and M_1 phases with non-spin-polarized (NSP), antiferromagnetic (AFM), and ferromagnetic (FM) ordering. The lowest ground state for GGA is a ferromagnetic R phase having a $1\ \mu_B$ moment while the temperature-dependent magnetic susceptibility measurements suggest that the R phase is a Curie-Weiss like paramagnetic metal with local moments [20, 92]. Initializing structural relaxations within the M_1 structure in an antiferromagnetic configuration yields a NSP state sustaining the dimerization, whereas FM initialization substantially reduces the dimerizaton from 0.653 $\mathring{A}$ to 0.191 $\mathring{A}$. None of the aforementioned phases within GGA possesses a band gap. As a next step, we study the phase stability with increasing U. The spin-polarized solutions quench dimerization in the M_1 phase, fully relaxing back to the R phase, whereas the lowest energy states for the R phase at $U = 1$ and 2 eV are ferromagnetic and antiferromagnetic ordered states, respectively. If we restrict ourselves to the NSP results, the M_1 phase is lowered relative to the R phase as U is increased, with the energetic ordering reversing for $U = 1$ eV.

LDA is also employed to investigate the relative energetics. No magnetic phases are stable within LDA, in the R or the M_1 phase. In all cases, the M_1 phase relaxes back to the R phase.However, as U is increased, the R phase becomes magnetic and the lowest

energy state is ferromagnetically ordered. At $U = 1$ eV, the M_1 phase remains NSP with the correct dimerization whereas the R phase has ferromagnetic ordering in the ground state, in agreement with experimental [18, 92]. However, the energy ordering between the R and M_1 phases is reversed and the M_1 phase is not gapped. At $U = 2$ eV, the ferromagnetic ordering of the R phase is still the ground state and the M_1 structure has a non-spin-polarized gapped state but the energy ordering is grossly reversed. Alternatively, restricting ourselves to NSP solutions for both the R and M_1 phases results in the correct energetic ordering.

Our calculation shows that the inclusion of U while obtaining the proper ground state (i.e. magnetic ordering) destroys dimerization, resulting in a reversed energy ordering of the R and M_1 phases and an antiferromagnetic ground state. This is in complete contradiction with experiment. The scenario gets progressively worse as the on-site interaction increases. On the other hand, NSP DFT($+U$) sustains the dimerization of the monoclinic phase as shown in the recent NSP DFT($+U$) studies [52, 57, 59] , giving a reasonable baseline for VO_2. Furthermore, NSP GGA nearly captures the insulating phase that occurs with a_{1g} orbital splitting while incorporating U reproduces the proper gap, as pictured in Figure 4.2. These NSP DFT+U predictions are rationalized by the fact that NSP and NSP Hartree-Fock solution are rather similar to the Peierls-Hubbard model, as stated in Section 3.5. It should be noted that constraining DFT+U to be NSP is unreasonable, but our results from the Peierls-Hubbard model demonstrate why this strange practice makes sense for this particular system.

However, there are a few theoretical observations that are not expected from the structural energetics of the Peierls-Hubbard model. While one might infer from the Peierls-Hubbard model, where NSP Hartree-Fock solutions have a fixed dimerization energy regardless of the size of U, that NSP solution of DFT+U should possess the fixed energy difference between the R and M_1 phases as a function of U, DFT($+U$) predicts that enhancing the on-site interaction U enlarges the energy difference, as shown in Figure 4.2. Furthermore, the metastable M_1 phase from GGA and LDA+U(= 1 eV) strongly suggest the importance

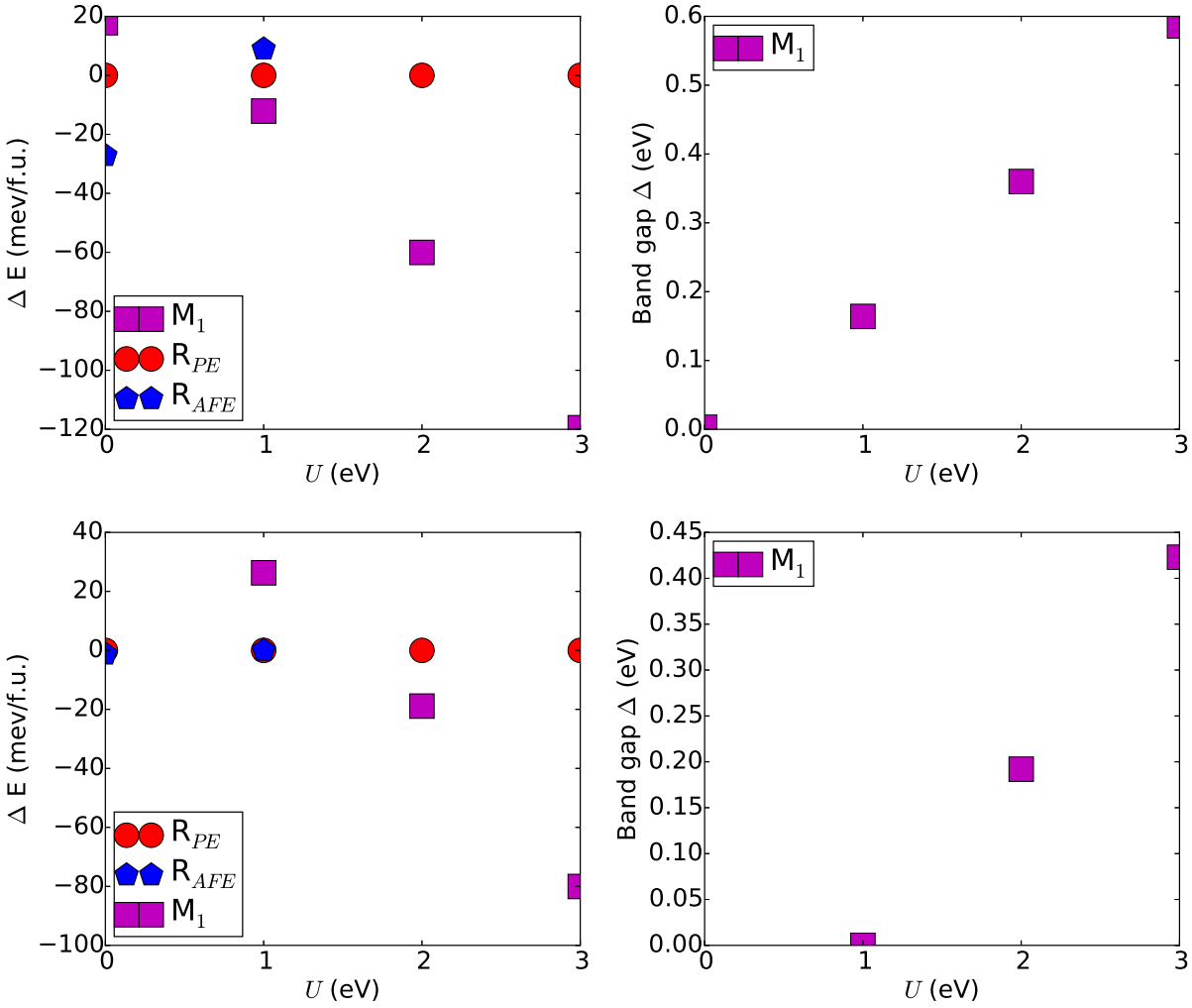

Figure 4.2: NSP DFT($+U$) is employed to study the effect of U on the dimerization energy and band gap of M_1. All phases are either stable or metastable in the sense that the crystal structures consisting of 4 atoms per unit cell is geometrically fully relaxed, allowing crystal symmetry breaking.

of orbital configuration and filling. This is because the on-site Coulomb interaction affects result in different configurations and fillings of t_{2g} orbitals that alter the low-energy physics of VO_2. On top of that, GGA predicts a metastable M_1 phase higher in energy than the R phase. This metastable M_1 phase is also a robust non-magnetic state that is stable against magnetic moment perturbations. We initialized the M_1 phase with magnetic moments of up to 4 μ_B (with both FM and AFM ordering), and it relaxes back to the NSP state and M_1 structure. Furthermore, both LDA and GGA predict that the lowest-energy magnetic state for the R phase is FM rather than AFM, whereas including U stabilizes the AFM solution. These predictions suggest that the multi-orbital nature can modify the simple picture of the Peierls-Hubbard model. Our LDA(+U) and GGA(+U) calculations corroborated their failures of LDA(+U) and GGA(+U) in describing the VO_2 transition whereas the proper restriction and modification to DFT solutions may qualitatively and semi-quantitatively capture many experimentally observed properties of the VO_2 transition.

While the unorthodox practice of using NSP DFT+U is promising, it must be noted that the on-site interaction U should be properly chosen. If U is too small, DFT+U has an antiferroelectric-like instability for the R phase (Figure 4.3). On the other hand, the charge ordering state is induced in the R phase when U is overwhelmingly large. Morever, GGA+U induces a gapped state in the R phase even within the NSP solution. Lastly, increasing U eliminates the barrier dictating the metastable R phase with the restricted NSP DFT+U solution, suggesting that the first-order nature of the transition might not be properly captured.

Furthermore, NSP DFT+U fails to predict the proper temperature dependence of phonons in the R phase. A recent neutron scattering study [57] found that the phonon spectrum (specifically, the acoustic phonon modes) of the R phase remains relatively fixed as a function of temperature, inconsistent with the observation of soft modes predicted by DFT+U at zero temperature (Figure 4.4, 4.5, and 4.6). Furthermore, it is a first-order phase transition so one can expect that the R and M_1 phases are metastable and can be described

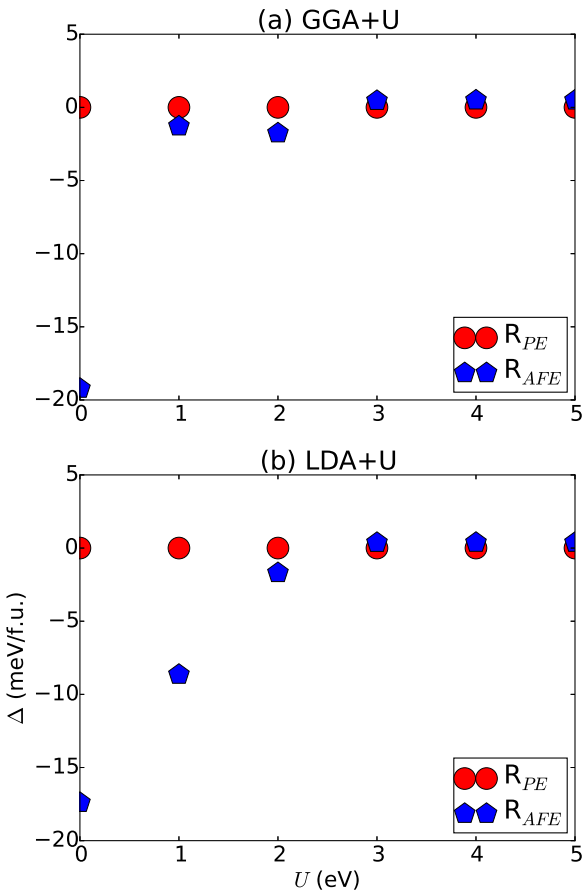

Figure 4.3: Antiferroelectric-like instability in the R phase is studied with (a) GGA+U and (b) LDA+U. The crystal structures consisting of two atoms per unit cell are employed.

within the harmonic approximation. However, recent studies suggest strong anharmonicity based on NSP DFT+U calculations, yielding an energy difference of 21.9 meV/atom at T = 0K and 11 meV/atom at the transition temperature [52, 57, 59]. In order to identify the major source of anharmonicity, we applied the decoupled anharmonic mode approximation to VO_2. Assuming that each phonon is independent of the others, the energy as a function of amplitude of each phonon mode can be employed to build partition functions to obtain the free energy of the system. From the decoupled anharmonic mode approximation [93], we were able to show that the R phase has a strong soft phonon at $\vec{q}$ = (1/4,0,1/4) and (1/4,0,1/2) (Figure 4.5 and Figure 4.7) which cannot be treated harmonically whereas the M_1 phase is harmonic and does not have soft phonon modes. The former is a major source

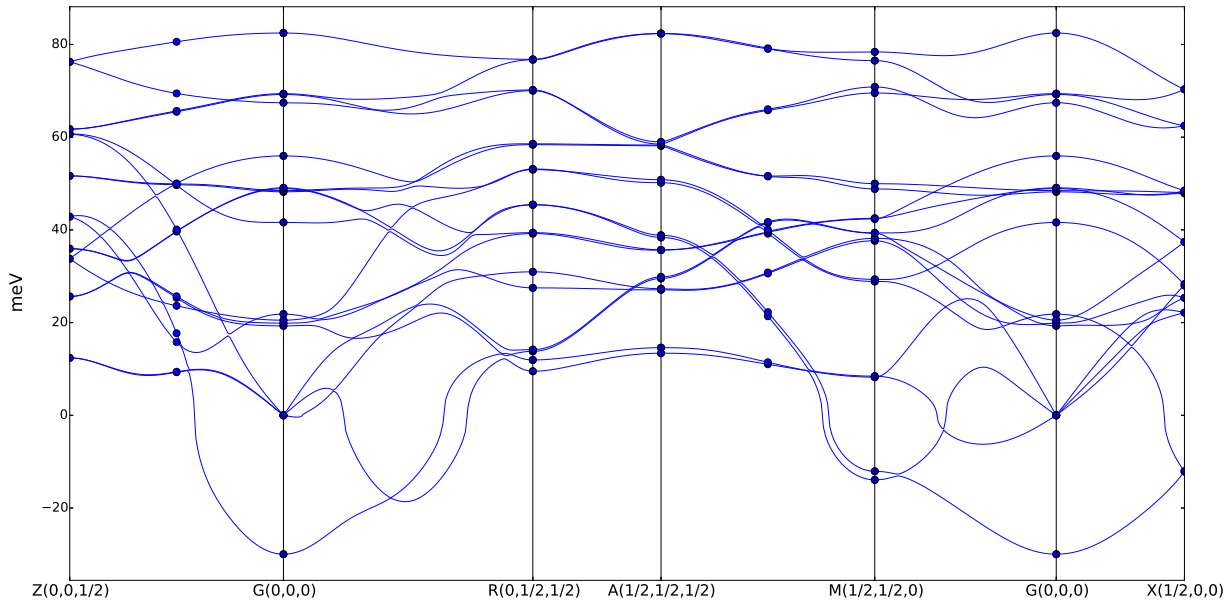

Figure 4.4: Phonon dispersions of the R phase for GGA are computed within the harmonic approximation. Negative energies indicate soft phonons. The supercell used is $2 \times 2 \times 4$. Lines and circles are computed by Fourier interpolation and frozen phonon method, respectively.

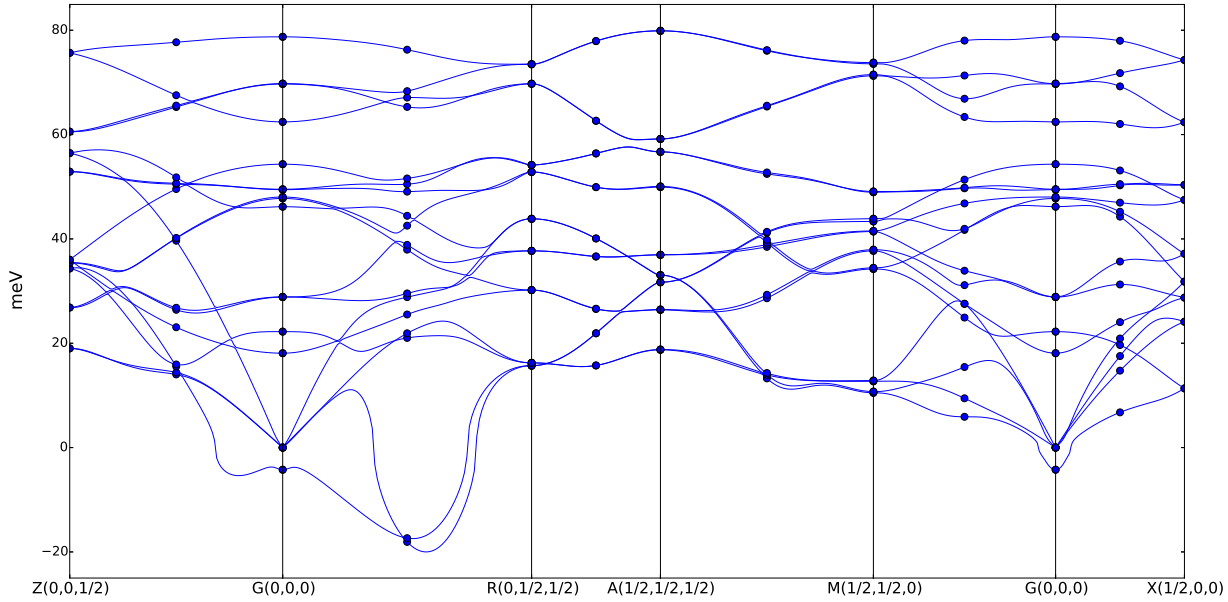

Figure 4.5: Phonon dispersions of the R phase for GGA+U(= 3.15 eV)+J(= 0.6 eV) are computed within the harmonic approximation. Negative energies indicate soft phonons. The supercell used is $4 \times 4 \times 4$. Lines and circles are computed by Fourier interpolation and frozen phonon method, respectively.

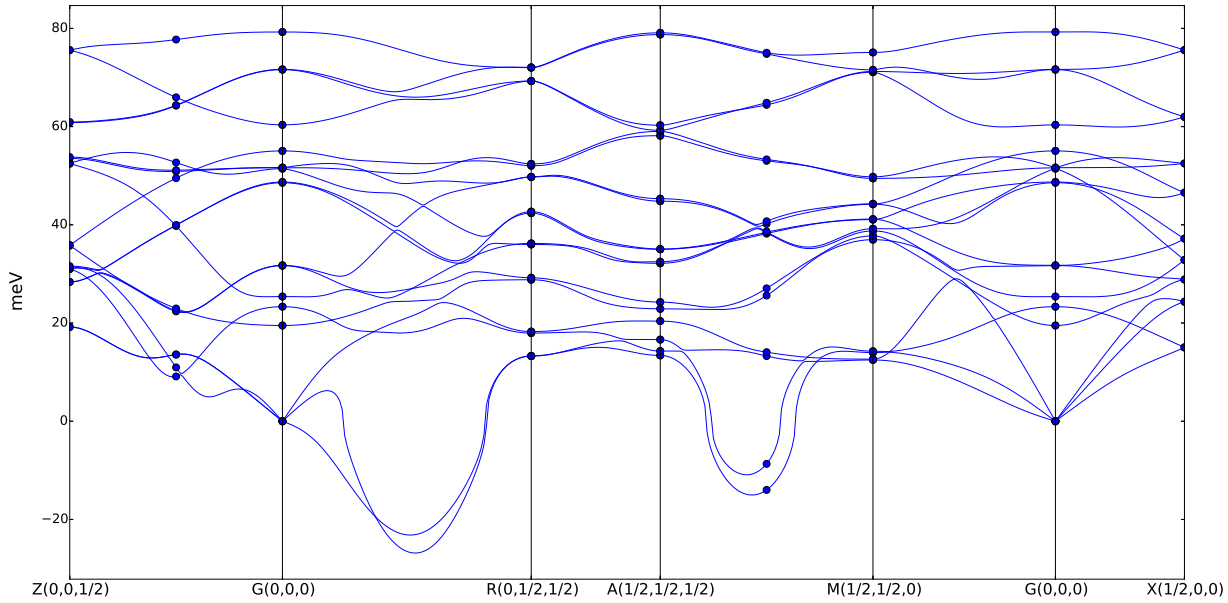

Figure 4.6: Phonon dispersions of the R phase for GGA+U(= 4.2 eV)+J(= 0.8 eV) are computed within the harmonic approximation. Negative energies indicate soft phonons. The supercell used is 2 × 2 × 4. Lines and circles are computed by Fourier interpolation and frozen phonon method, respectively.

of anharmonic effects in the thermodynamics of VO_2. However, these soft modes are not consistent with the temperature-dependent phonons measured in neutron scattering. Therefore, adjusting the U parameter alone is not sufficient to attain a full understanding of the VO_2 transition from first principles.

4.2 Single-particle density matrix extension to DFT(+U)

In the previous section, we identified that even NSP DFT+U has discrepancies with experiment. While the NSP DFT+U solution gives a baseline, further tweaking within the effective single-particle density matrix is required to control the orbital configuration and filling. We use parameters α and β in the equation $E = E_{DFT+U} + \alpha(N_{e_g^\pi} - N_{a_{1g}}) + \beta N_d$ to fine-tune DFT+U for describing the phase transition of VO_2. The parameter α controls the crystal

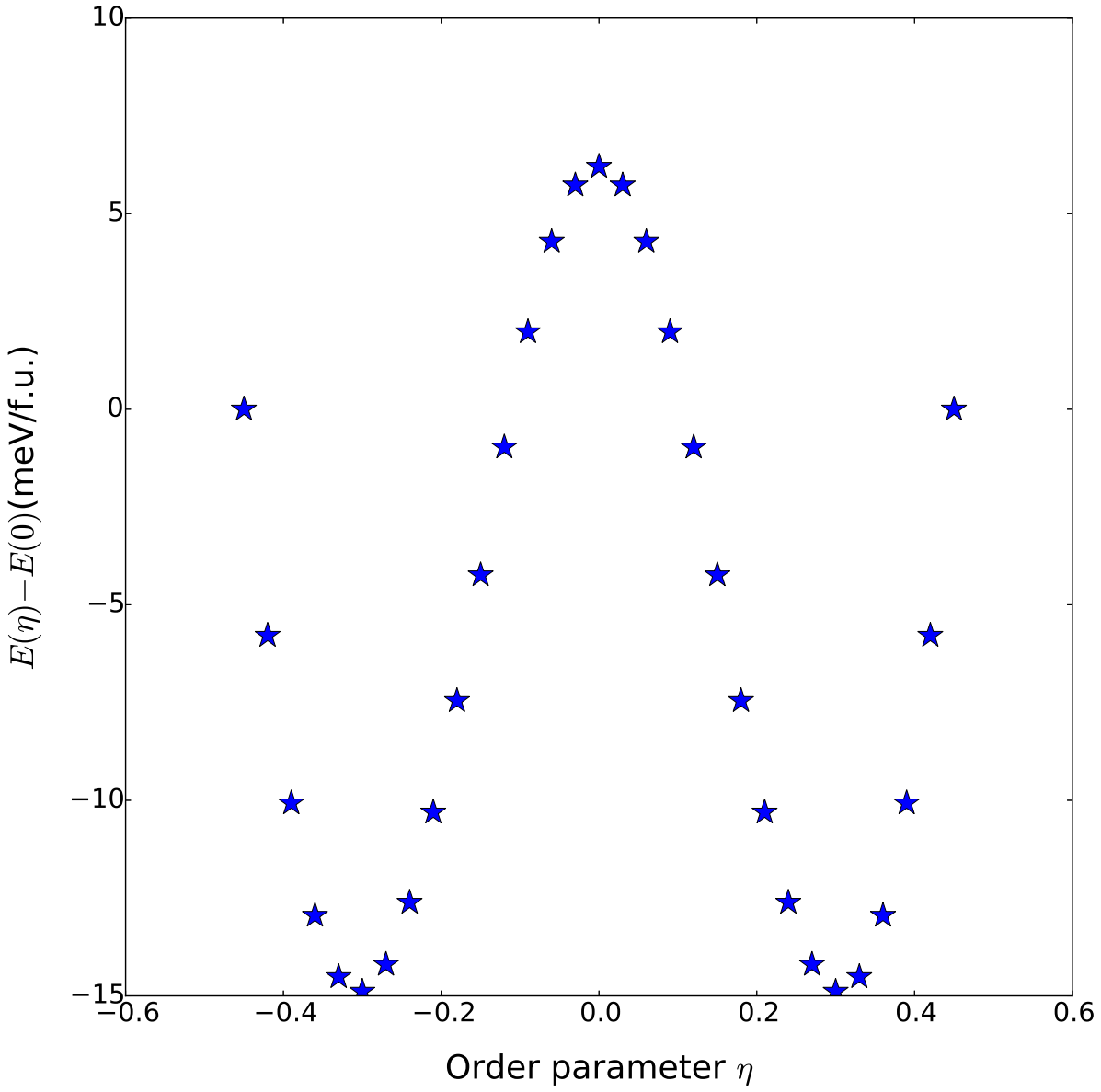

Figure 4.7: Total energy versus order parameter of $\vec{q}$=(0.5,0,0.25) phonon for GGA+U(= 3.15eV)+J(= 0.6eV)

splitting between a_{1g} and e_g^π whereas β determines the charge transfer between the oxygen 2p and vanadium 3d orbitals. Furthermore, we will study how the orbital configuration and filling changes via α and β influence the structural energetics. Similar studies have shown promising results for the phase stability of R, M_1 and M_2 through DFT embedded with an orbital-depedent static potential using the experimental structures, which are fixed [39]. This computational results confirm the importance of orbital polarization in a multi-band scenario[5]. However they did not fully account for the electron-phonon coupling in their computation via geometrical optimization, which is critical to the structural energetics. We have modified the VASP code to incorporate a single-particle matrix consisting of α and β in addition to DFT+U.

The crystal field α penalizes the filling of e_g^π and enhances the filling of a_{1g}. According to the photoemission data [94], the metallic phase has evidence of strong local interactions that induce a clear polarization between the a_{1g} and e_g^π orbitals. Single-site DMFT suggests an artificial crystal field induced by an antiferroelectric displacement of V^{+4} ion is critical to obtain an insulating phase, highlighting the importance of orbital mixing in the VO_2 phase transition[42]. Cluster DMFT repeatedly predicts that the correlations of the R phase take electrons out of e_g^π band to enhance the a_{1g} band filling (i.e. 0.42 for a_{1g} and 0.29 for e_g^π) compared to almost equally distributed occupancies of t_{2g} by LDA (i.e. 0.36 for a_{1g} and e_g^π for 0.32) [41]. Furthermore, the anisotropic electronic transport (resistivity) has been observed by Bongers [95] and evidences the orbital polarization between t_{2g} orbitals even in the metallic phase [5, 6]. A theoretical study suggests that biasing e_g^π lowers the energy of dimerized states relative to undimerized ones [96]. This scenario is upheld by an experimental study demonstrating that the relative configuration of t_{2g} orbitals in the metallic phase is critical to the energy scale of the metal-insulator transition [6].

On the other hand, the parameter β is closely related to the double-counting problem in methods beyond DFT. It shifts the total filling of the d-shell and has been shown to be important in attaining the correct structural energetics of several correlated materials.

In VO_2, the p-d charge transfer determines whether metal-metal bonding or metal-oxygen bonding wins out. The p-d splitting is experimentally observed to be 1.5 eV for the R phase and 0.4 eV for the M_1 phase [97], and experimental measurements from x-ray absorption spectroscopy find d-orbital occupancy N_d to be $1.78e^-$ [5]. On the other hand, NSP calculations via DFT($+U$) show a narrower p-d charge transfer and thus larger N_d filling. Whereas the NSP GGA+U solution tends to result in a narrower p-d splitting than it should have, the movements of soft phonons in the NSP GGA+U phonon calculations are consistent with the theoretically predicted antiferroelectric-like instability in which V atoms move out of the center of the octahedron in the metallic R phase. Our calculations show that such instabilities harden and become harmonic with increasing β. One may argue that antiferroelectric-like instabilities occur in VO_2 when the p-d splitting is not sufficiently large. However, the instabilities likely do not exist in reality and are likely an artifact of the method due to the smaller p-d splitting predicted by NSP DFT+U. Therefore, we need to carefully control β in addition to α and U.

Although the three different knobs have their own independent physics, they do interact with each other. In particular, changing U will directly alter α and β. Their effects on the structural energetics of the VO_2 phase transition should be considered as a whole. Given that exploring a three-dimensional space has a nontrivial computational cost, we use non-charge self-consistent calculations to scan the phase space and hone in on proper parameters before fine tuning further. The relationship between α and β as studied by non-charge-self consistent calculations is shown in Figure 4.8. Specifically, while a larger α helps stabilize the dimerized structure, a larger β is needed to sustain a paraelectric R phase that is lower in energy than the antiferroelectric-like R phase. It holds conversely as well. Given that non-charge-self-consistent calculations only hold with small changes in α and β, performing charge-self-consistent calculations is a necessary condition to finalize the parameters to be employed. It should also be noted that the crystal volume increases dramatically when α gets too large. After iteratively tuning the parameters, we ultimately determined that (U,

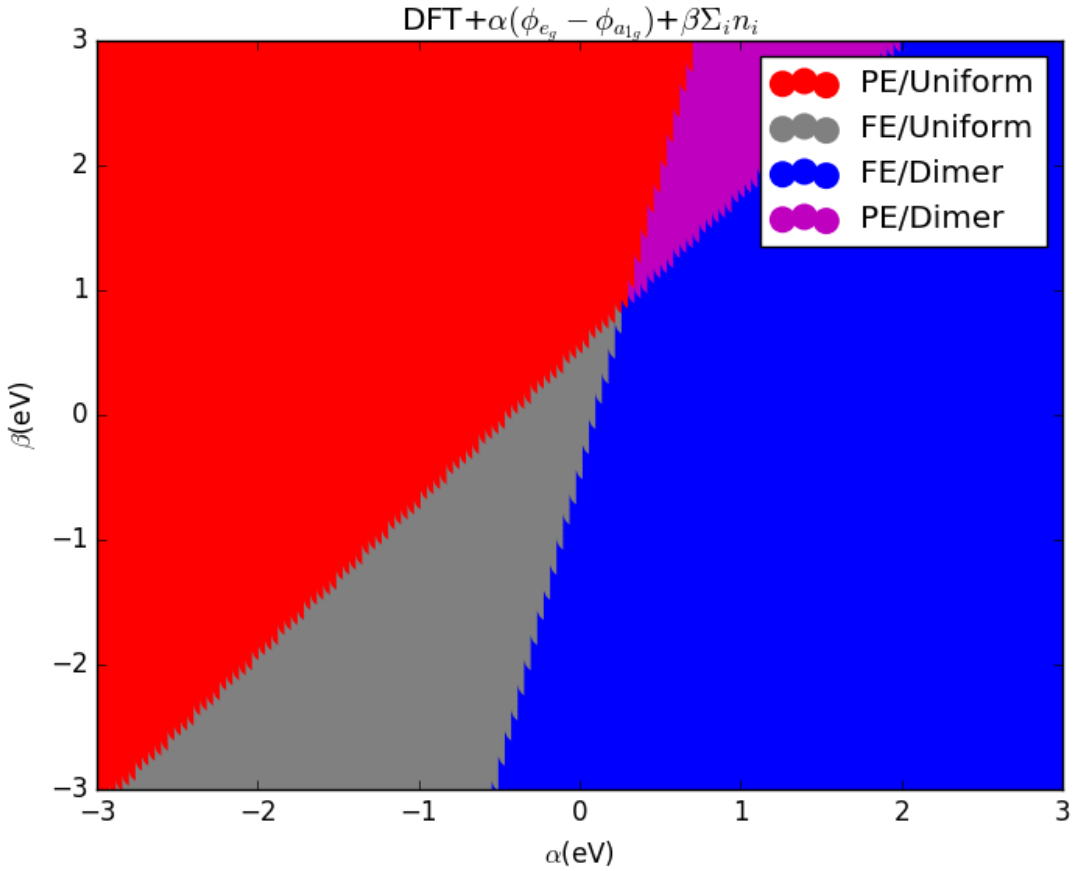

Figure 4.8: Phase stability of paraelectric R phase, antiferroelectric-like R phase, dimerized M_1 phase, and undimerized M_1 phase as a function of α and β

α, β) = (1.0 eV, 0.35 eV, 1.6 eV). Their validity will be documented in the next chapter.

Chapter 5

Predicting the phase diagram of VO_2 from first principles

In the previous chapter, we designed a single-particle matrix functional and came up with an interpretation of DFT($+U$) results based on the Peierls-Hubbard model, demonstrating the importance of the strong one-dimensional nature of the a_{1g} orbital and its interaction with other orbitals. In this chapter, we validate its predictability for a variety of experimental observables in the phase transition of VO_2. First, we predict the crystal structures and electronic structures of both the R and M_1 phases at T = 0K and the energetics of the transition along the reaction pathway. Next, we compute the phonon spectra of both phases within the harmonic approximation, manifesting the metastability of the R phase. Furthermore, we predict the phase diagram of the R-M_1 phase transition in VO_2. The results of the single-particle matrix functional are compared with experimental observations.

We utilize a single-particle matrix functional to compute the crystal structures of the R and M_1 phases (Figure 5.1) and compare the results with other conventional approaches such as LDA, GGA, and their Hubbard U corrections, where all methods are forced to be NSP (Table 5.1 and Table 5.2). DFT+$U+\alpha+\beta$ successfully captures the dimerization in the M_1 phase. Our functional predicts slightly larger volumes for both the R and M_1 phases

Table 5.1: A summary of structural features of the R phase in experimental and theoretical observations. Both LDA+U and GGA+U use 2 eV for the onsite Coulomb interaction. The space group is $P4_2/mnm$ and experimental parameters are reproduced from [19].

Functional	LDA	LDA+U	GGA	GGA+U	LDA+U+α+β	EXP
a($\mathring{A}$)	4.47	4.49	4.58	4.60	4.66	4.5546
c($\mathring{A}$)	2.83	2.83	2.83	2.83	2.80	2.8514
V($\mathring{A}^3$)	56.66	57.17	59.52	60.09	61.06	58.151

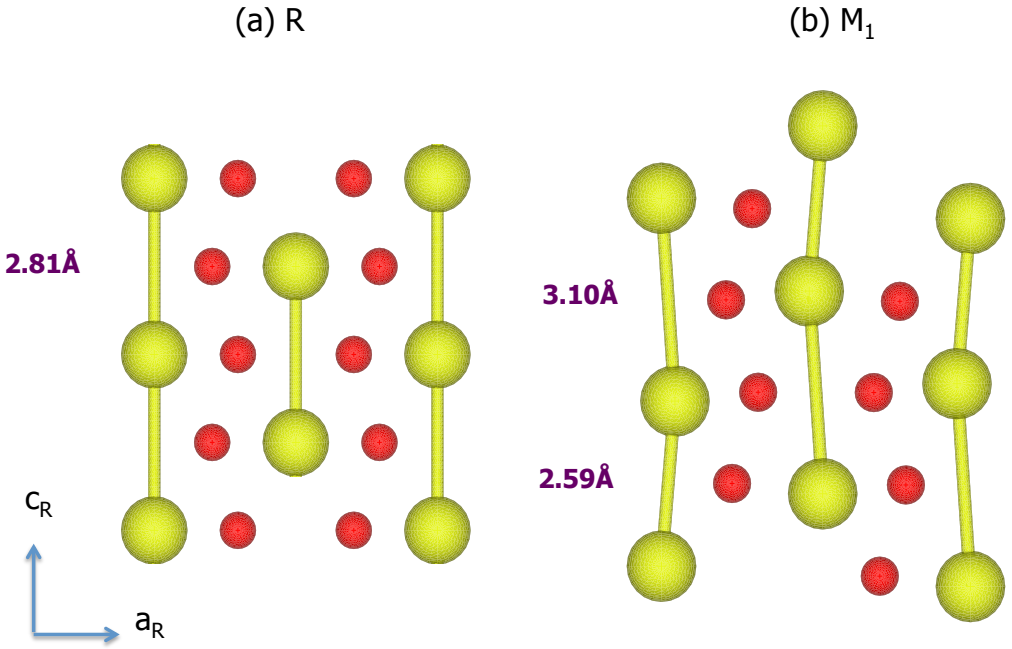

Figure 5.1: The crystal structure of (a) the R and (b) the M_1 phases predicted by a single-particle density functional

Table 5.2: A summary of structural features of the M_1 phase in experimental and theoretical observations. Both LDA+U and GGA+U use 2 eV for the onsite Coulomb interaction. The space group is $P2_1/c$ and experimental parameters are reproduced from [21]. δ is the degree of dimerization defined as the long bonding length of V-V subtracted from the short bonding length.

Functional	LDA	LDA+U	GGA	GGA+U	LDA+U+α+β	EXP
a($\mathring{A}$)	N/A	5.50	5.64	5.62	5.67	5.75
b($\mathring{A}$)	N/A	4.53	4.60	4.62	4.63	4.54
c($\mathring{A}$)	N/A	5.31	5.41	5.44	5.44	5.38
$\beta(^\circ)$	N/A	121.46	121.78	121.78	121.55	122.65
V($\mathring{A}^3$)	N/A	112.71	118.91	119.98	121.81	118.29
δ ($\mathring{A}$)	N/A	0.597	0.653	0.659	0.510	0.545

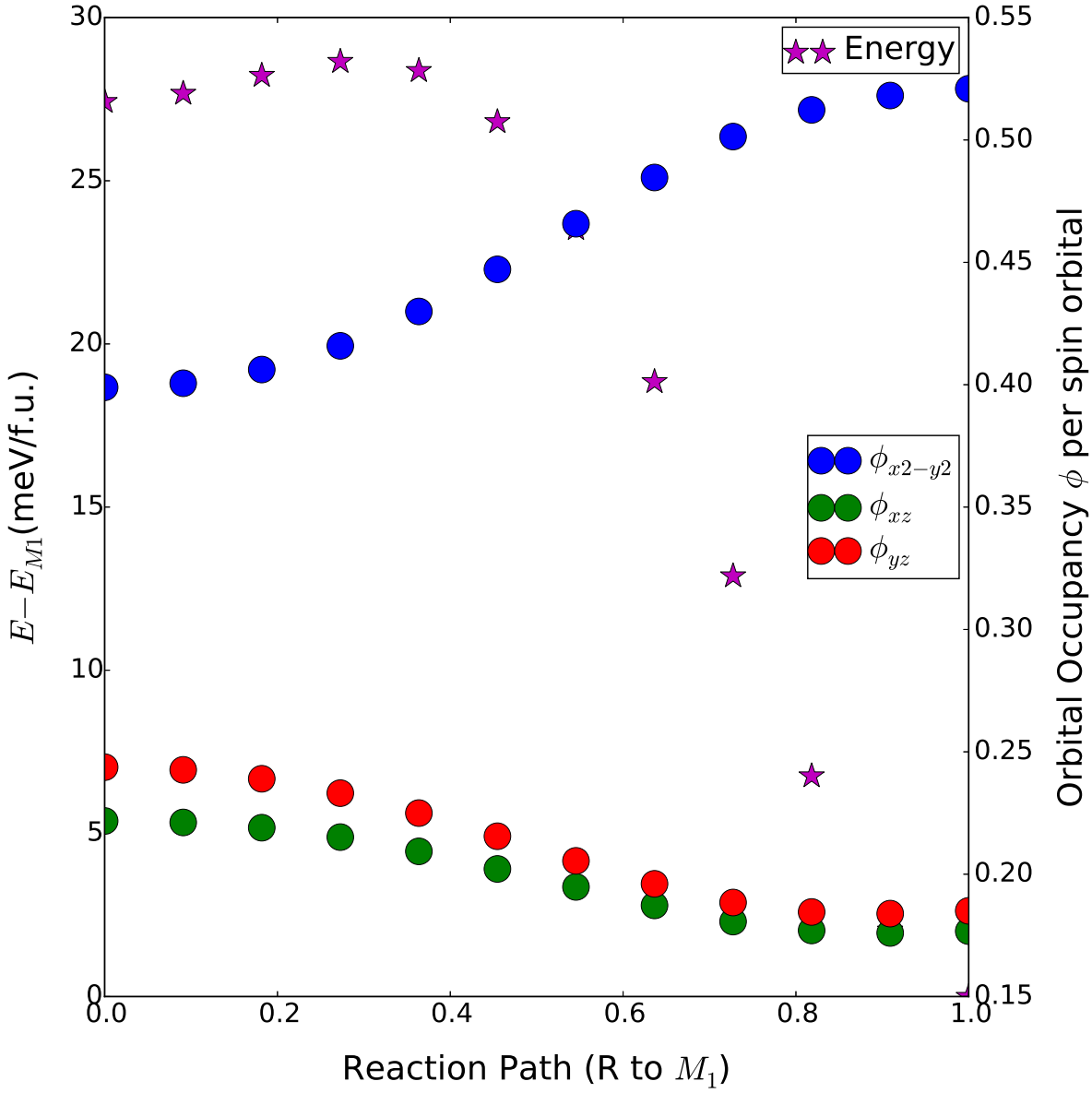

Figure 5.2: Stars represent the energy relative to the M_1 phase along the transition. Circles represent occupancies of a_{1g} and e_g^{pi} per spin orbital.

compared to other conventional functionals, but the dimerization is in better agreement in experiment. In general, the crystal structural parameters of the predicted R and M_1 phases are in reasonable agreement with experimental observations.

The structural energetics are computed along the reaction pathway between the R and M_1 phases via linear interpolation (Figure 5.2). The phase stability of the R and M_1 phases

is in qualitative and semi-quantitative agreement with experimental observations. Each phase is metastable as dictated by the barrier, which comes from the multiband nature of both a_{1g} and e_g^π, where e_g^π removes electrons from the a_{1g} orbitals and penalizes the Peierls distortion. This barrier makes the transition first-order with a rather high transition temperature, whereas a pure a_{1g} electron correlation mechanism might have led to a second-order transition. This argument is supported by the change in occupancy of a_{1g} and e_g^π orbitals during the transition.

The electronic density of states for both the R and M_1 phases is also calculated (Figure 5.3). The R phase shows metallic behavior while the M_1 phase has a 0.07 eV gap. The calculated gap of the M_1 phase is smaller than from that experimental observations, but this is expected from the Peierls-Hubbard model in the sense that a_{1g} splitting created by non-spin-polarized Hartree-Fock solutions for the Peierls-Hubbard model is, in fact, very weak compared to the splitting predicted by its exact solution from the density matrix renormalization group. Since the gap of the M_1 phase in VO_2 is dictated by the electronic energy spacing between the split lower bands of a_{1g} and the upshifted e_g^π bands, one can infer that the size of the a_{1g} splitting is a critical component in determining the size of gap. This observation may explain why our designed functional predicts a smaller gap despite properly capturing the structural energetics. We are thus able to show that the single-particle density functional captures the qualitative and semi-quantitative picture of both structural and electronic properties of the R and M_1 phases.

Furthermore, Figure 5.4 shows that a single-particle density functional produces a harmonic phonon spectrum of the R phase without any soft phonon modes, and the only zone-edge $\langle 101 \rangle$ phonon becomes unstable if the thermal energy is sufficiently large to overcome the barrier. This is in agreement with experimental observations in the sense that the acoustic phonon modes at the R point are minimally changed but renormalized to a new value above the transition temperature which is also weakly temperature-dependent [57]. The energy is plotted as a function of the amplitude of the combination of two lowest

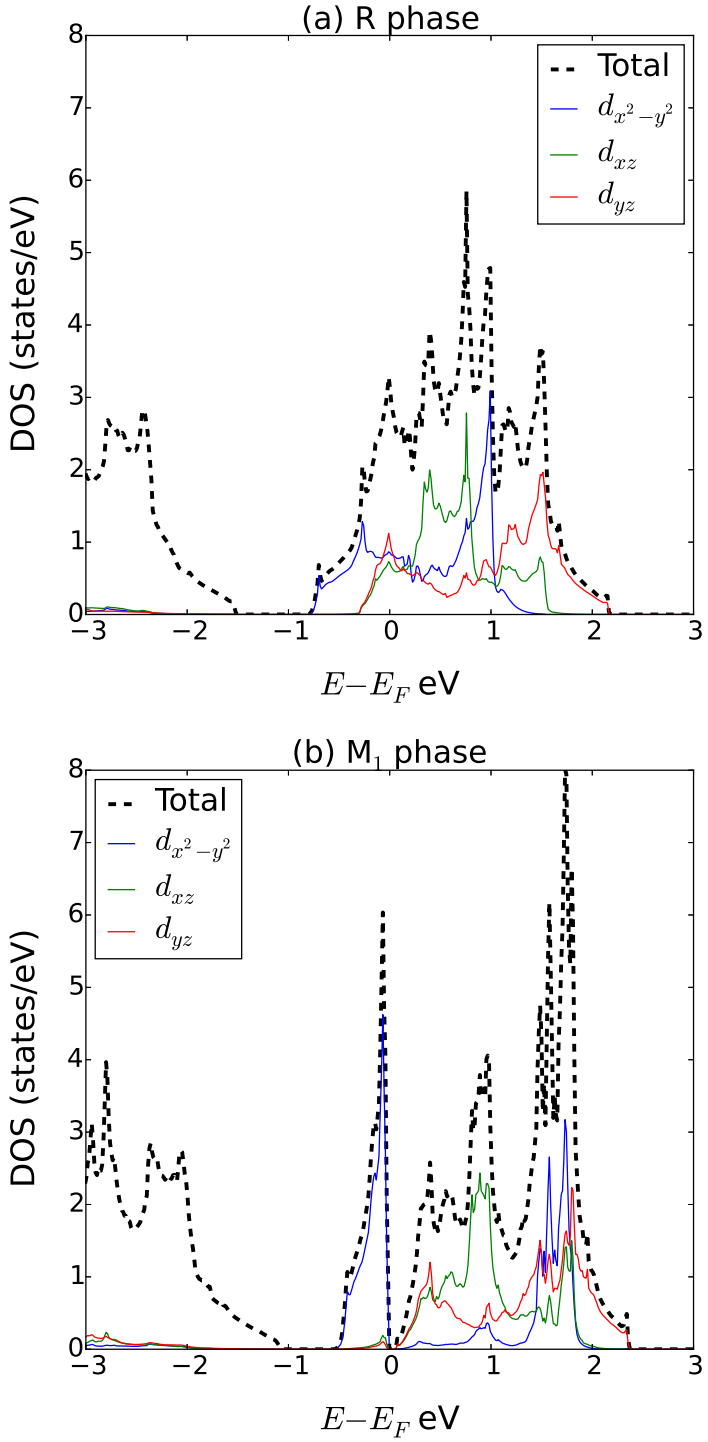

Figure 5.3: Electronic structure of (a) R and (b) M_1 phases via single-particle density functional. Total density of states and projected density of states for t_{2g} orbitals is plotted.

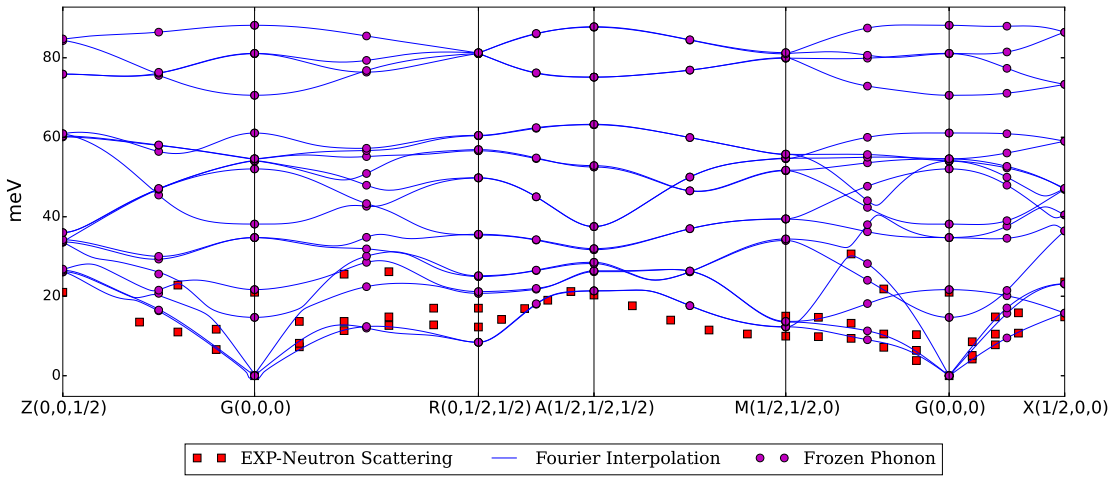

Figure 5.4: Phonon spectrum of the R phase is plotted along with experimental observations [57].

degenerate phonon modes ($\eta = \eta_1 + \eta_2$) at the R point in Figure 5.5, showing that it is consistent with an unstable $\langle 101 \rangle$ zone-edge phonon that is observed by x-ray diffuse scattering measurements [98] and predicted by symmetry considerations [99].

$$F = E - TS. \tag{5.1}$$

$$Z = \Sigma_i e^{-\beta E_i} \tag{5.2}$$

$$E = -\frac{\partial}{\partial \beta} \ln(Z) = k_B T^2 \frac{\partial}{\partial T} \ln(Z) \tag{5.3}$$

$$F = -k_B T \ln(Z) \tag{5.4}$$

$$S = -k_B \ln(Z) - k_B T \frac{\partial}{\partial T} \ln(Z) \tag{5.5}$$

It has long been known, however, that the R phase has a large Debye-Waller factor which points to strong fluctuations in atomic positions [19, 100]. A recent study analyzed the phonon density of states in both phases, both experimentally and theoretically, and concluded that the R phase is stabilized through increased entropy due to phonon softening in

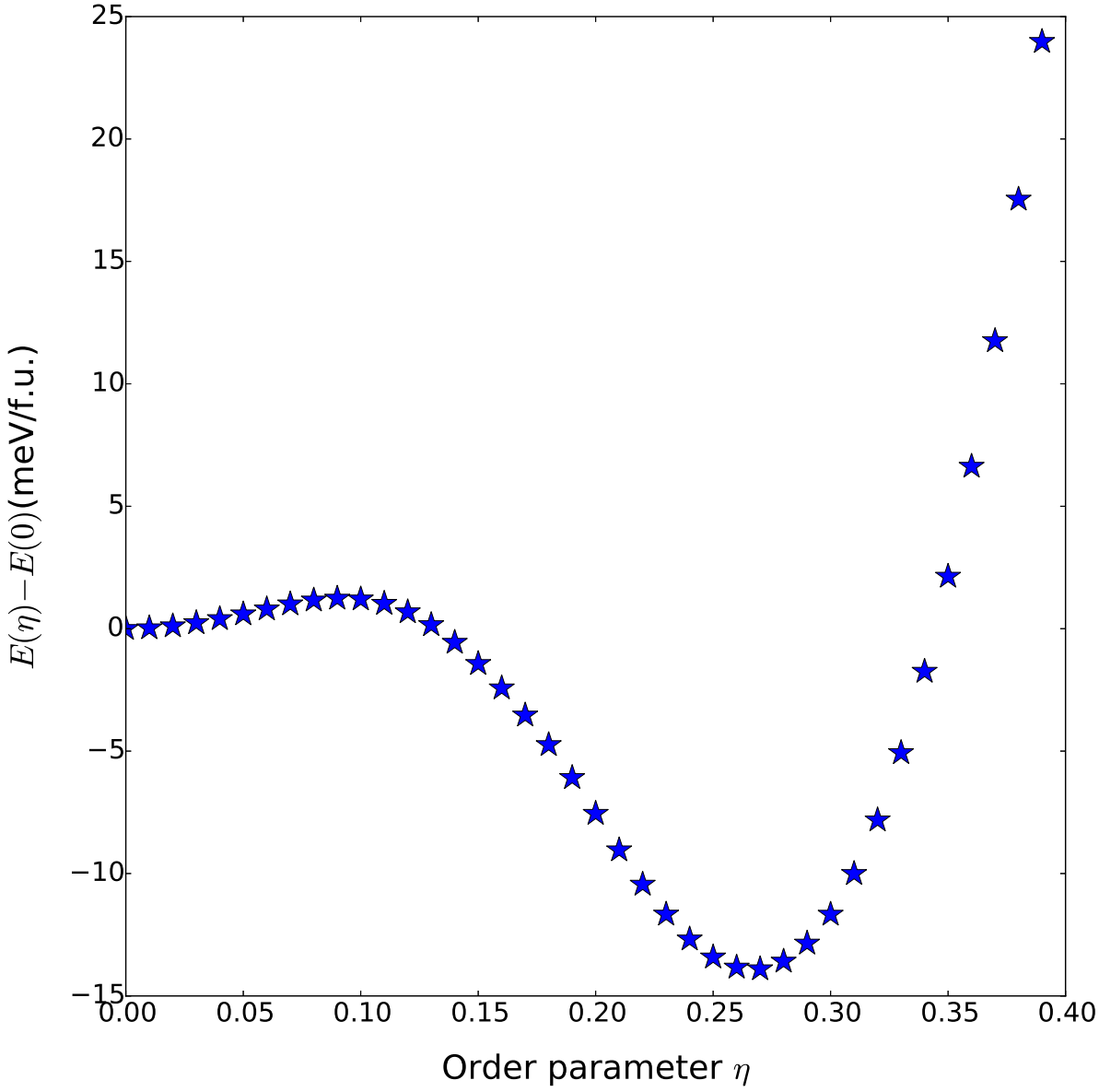

Figure 5.5: Total energy versus order parameter (η) of $\vec{q} = (0.5, 0, 0.5)$ phonon.

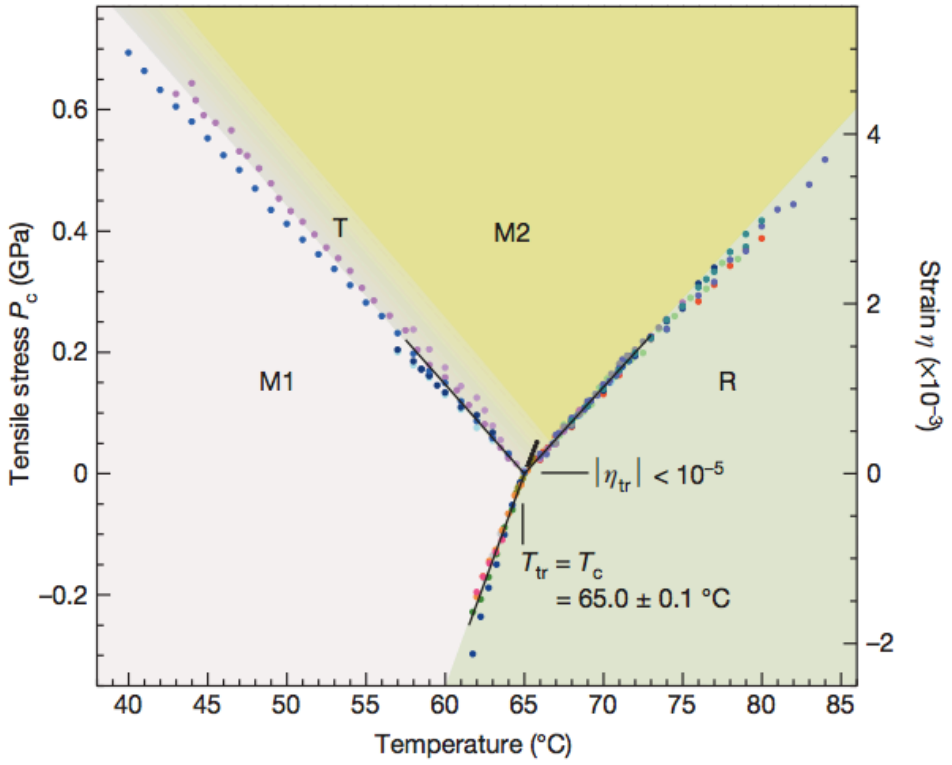

Figure 5.6: Nanobeam experimental result of the temperature-strain phase diagram of VO_2 reproduced from [17]

the metallic phase [57]. This means that with increasing temperature the lattice free energy decreases more rapidly for the metallic configuration and eventually the total free energy becomes lower for this phase. This scenario is evidenced by the phonon entropy calculation of both the R and M_1 phases, resulting in $2.33k_B$/atom and $2.07k_B$/atom, respectively. Free energy calculations performed by constructing partition functions further confirm the scenario described by Equations 5.1-5.5. In the harmonic approximation, the canonical partition function can be deduced in the form of $Z_\omega = \frac{e^{-\beta\hbar\omega/2}}{1-e^{-\beta\hbar\omega}}$ for each harmonic oscillator. The free energy is then derived as $F = -k_B T \ln(Z)$. Therefore, it is straightforward to compute the free energy difference as a function of temperature.

There have been many experimental studies on the effect of strain on the transition tem-

perature, all of which find a positive correlation between the strain along the c_r axis and the transition temperature, T_c [101, 102]. In 2013, a single-crystal VO_2 nanobeam experiment precisely controlled uniaxial stress on the VO_2[17]. It reproduces the known behavior of the temperature-strain phase diagram and provides a slope of transition temperature changes as a function of strain (Figure 5.6). The phase diagram implicitly indicates that a proper compressive stress will hypothetically produce the R phase at zero temperature. On the other hand, theoretically predicting the temperature-strain phase diagram of VO_2 from first principles has never been achieved so far. To the best knowledge of the author, there are only two first-principle studies pertaining to the phase transition temperature of bulk VO_2[57, 59], but neither studied the transition temperature as a function of strain.

We study the experimentally observed temperature-strain phase diagram by employing our single-particle density matrix functional. Strain values ranging from -2% to 0% are only predicted because the single-particle density functional restricts the spin-polarized solution and thus the M_2 phase should be excluded due to its magnetic ordering. The M_2 phase requires more advanced theories such as cluster-DMFT as shown in the model study. In order to properly induce a strain as in the nanobeam experiment, we applied strain along the x-axis, i.e. the pseudo c-axis, while fully relaxing the perpendicular strains. We identified a bond length for zero strain as the c-length of the fully relaxed M_1 phase, since the M_1 phase is the T = 0K crystal structure of VO_2. Due to the high computational cost, we selected only three points for the strain: -2%, -1%, and 0%. The phonon spectra of both the R and M_1 phases at each strain have been computed and are presented in Figures 5.7 - 5.12.

$$.\frac{F}{N} = \frac{E^*}{N} + k_B T \int_0^\infty \ln[2\sinh(\frac{h\nu}{2k_B T})] g(\nu) d\nu = \frac{E^*}{N} + \frac{k_B T}{N} \Sigma_m \ln[2\sinh(\frac{h\nu_m}{2k_B T})] \qquad (5.6)$$

None of the strain-dependent phonon spectra for the R and M_1 phases have a soft phonon mode and are described within the harmonic approximation. Therefore, the free energy of

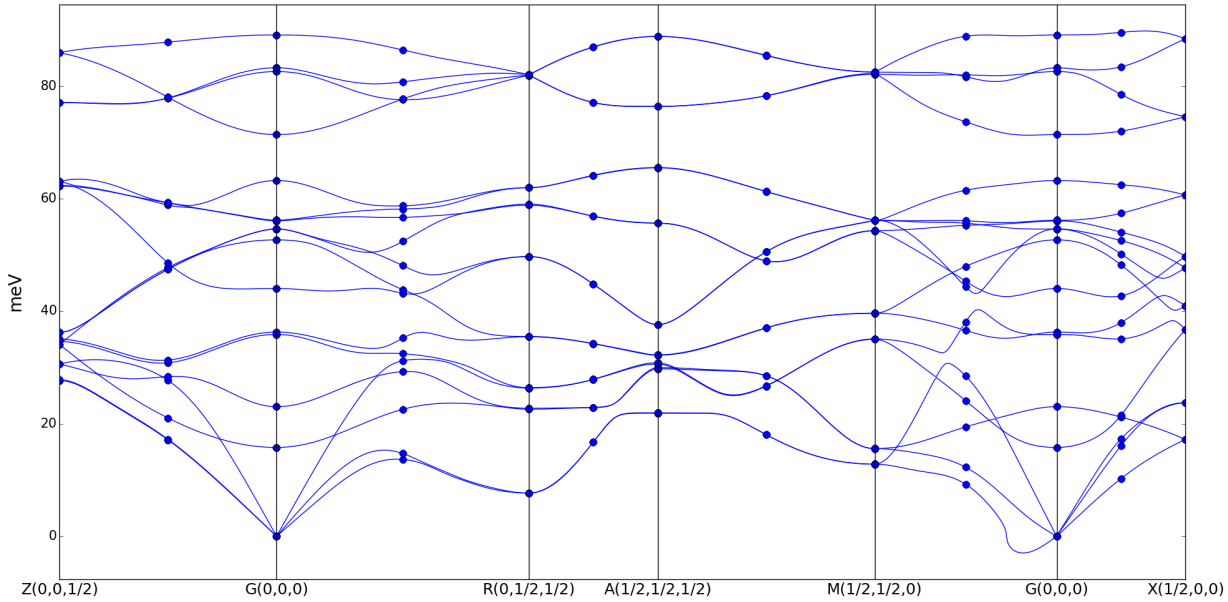

Figure 5.7: Phonon spectrum of the R phase at -2% strain computed by a single-particle density matrix functional. Lines and circles are computed by Fourier interpolation and frozen phonon method, respectively.

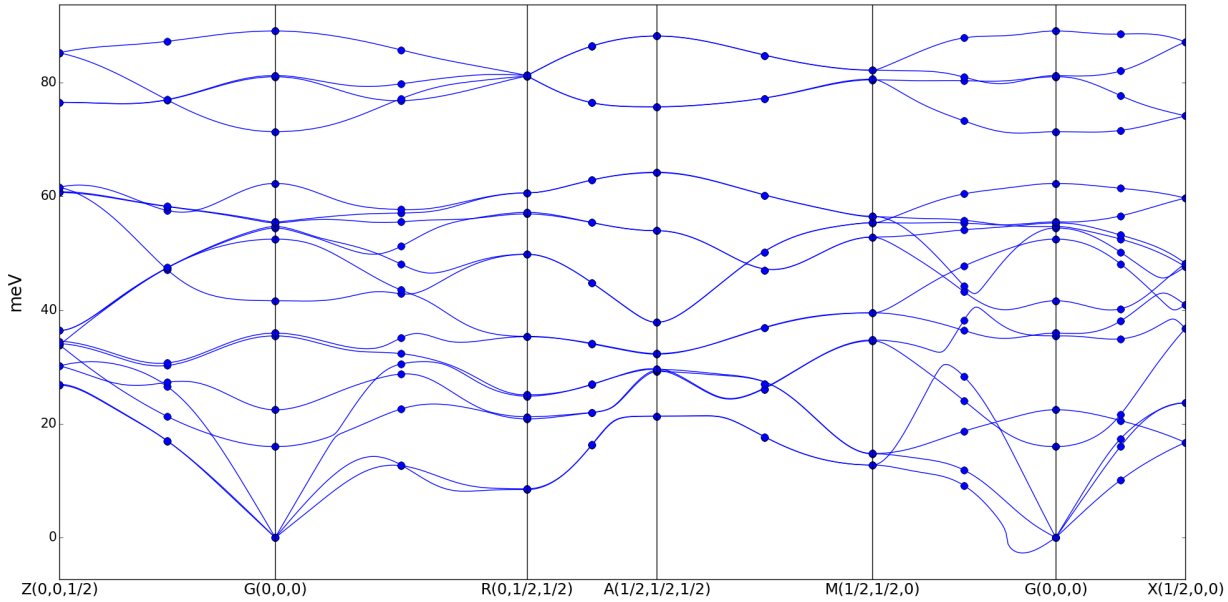

Figure 5.8: Phonon spectrum of the R phase at -1% strain computed by a single-particle density matrix functional. Lines and circles are computed by Fourier interpolation and frozen phonon method, respectively.

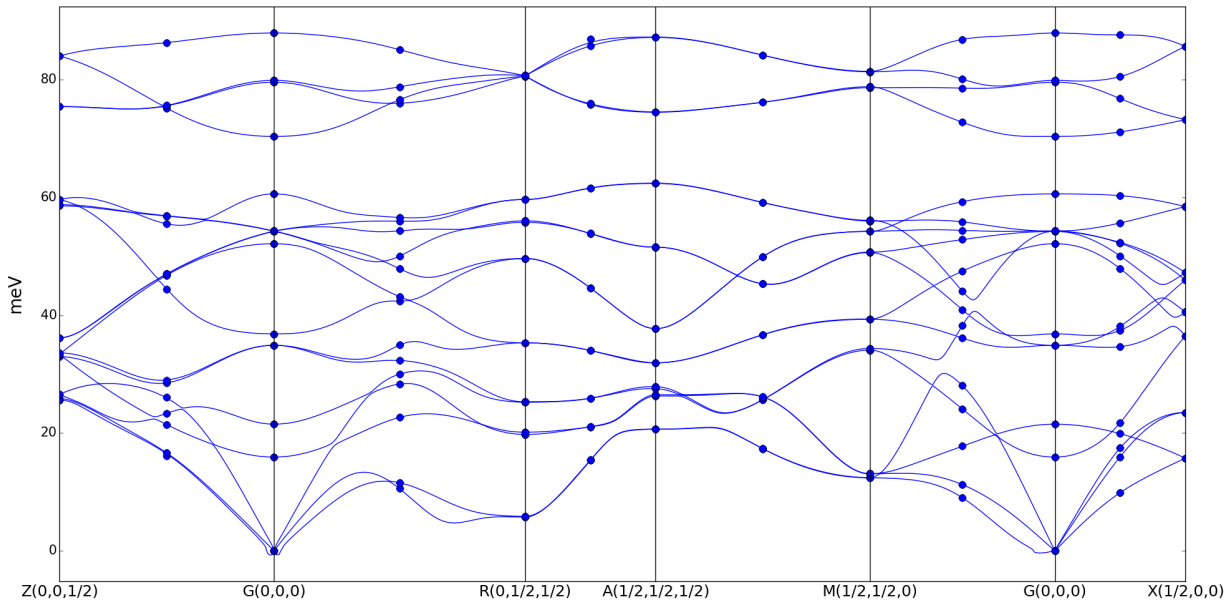

Figure 5.9: Phonon spectrum of the R phase at 0% strain computed by a single-particle density matrix functional. Lines and circles are computed by Fourier interpolation and frozen phonon method, respectively.

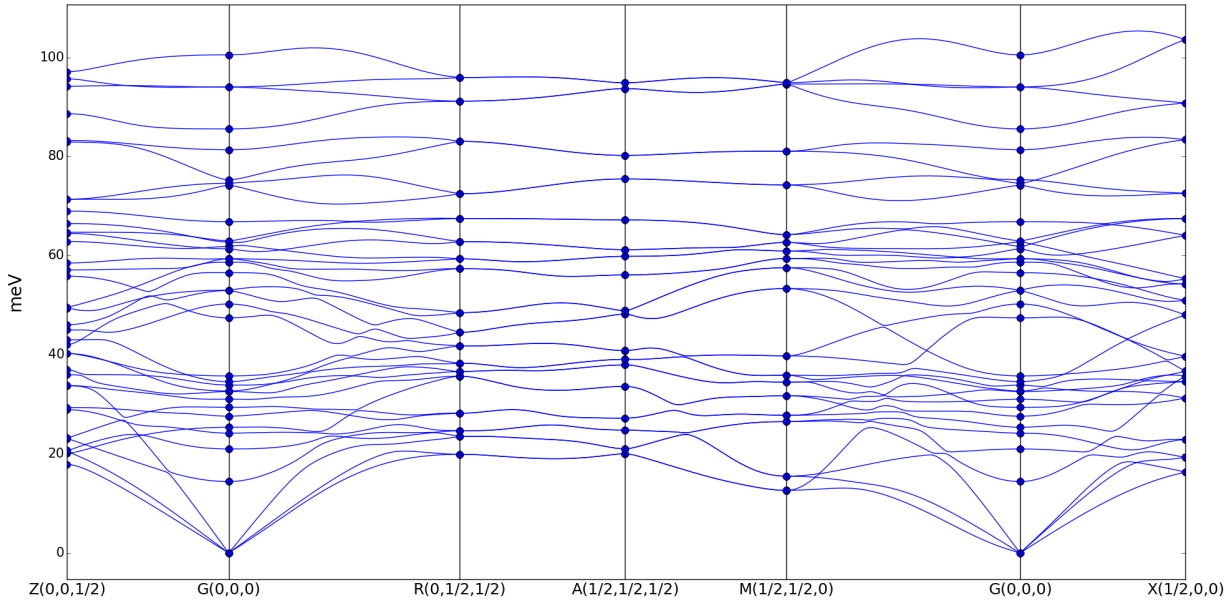

Figure 5.10: Phonon spectrum of the M_1 phase at -2% strain computed by a single-particle density matrix functional. Lines and circles are computed by Fourier interpolation and frozen phonon method, respectively.

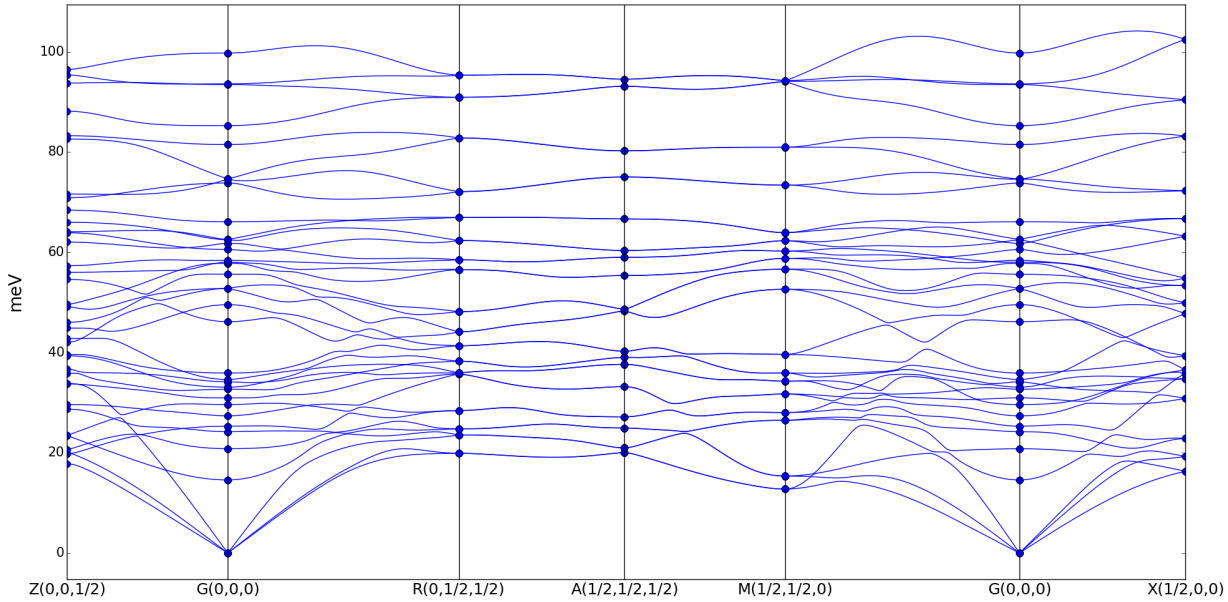

Figure 5.11: Phonon spectrum of the M_1 phase at -1% strain computed by a single-particle density matrix functional. Lines and circles are computed by Fourier interpolation and frozen phonon method, respectively.

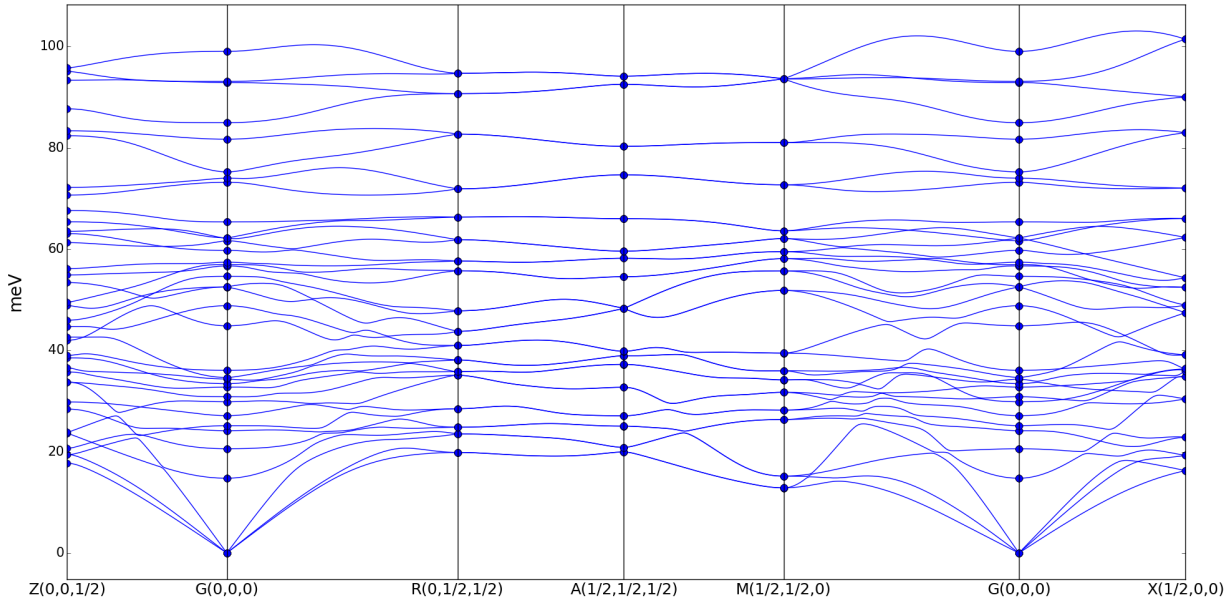

Figure 5.12: Phonon spectrum of the M_1 phase at 0% strain computed by a single-particle density matrix functional. Lines and circles are computed by Fourier interpolation and frozen phonon method, respectively.

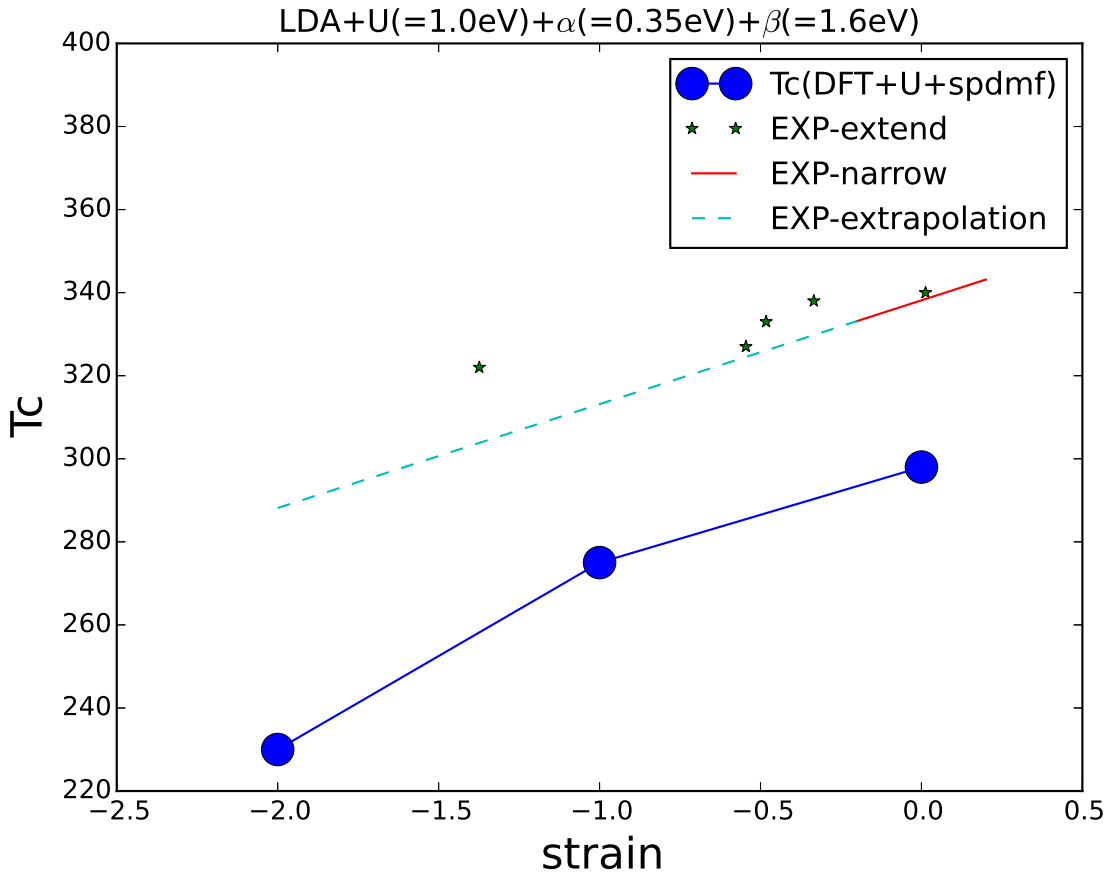

Figure 5.13: Temperature-strain phase diagram reproduced by a single-particle matrix functional. Experimental data reproduced from [17] for both EXP-narrow and EXP-extrapolation and [101] for EXP-extend

the system can be simply computed via Equation 5.6 [103]. The parameter E^* indicates the DFT energy of the system, while ν and $g(\nu)$ stand for the phonon frequency and phonon density of states, respectively. The phase transition occurs when the free energies of the R and M_1 phases become equal. The temperature-strain phase diagram is computed using a single-particle density functional and plotted as a function of strain in Figure 5.13. As the strain varies, the R phase remains metallic and the insulating gap of the M_1 phase changes minimally. Therefore, we only included phonon entropy to compute the free energy because the electronic entropy changes across strains should be minimal. It should be noted that our theoretical calculations predict the change of transition temperature between R and M_1

phase as a function of strain in qualitative and semi-quantitative agreement with experimental observations[17, 101]. This can be interpreted as evidence that strong electron-phonon coupling and lattice softening are crucial for the transition whereas electronic contributions are minimal.

Chapter 6

Conclusions and Outlook

We have reviewed numerous theoretical studies pertaining to the VO_2 phase transition carried out over the past several decades, emphasizing the importance of an advanced treatment of electron-electron correlations. We have found a lack of literature from the perspective of structural energetics in VO_2 due to the insurmountable costs associated with treating VO_2 using advanced methodologies such as the cluster extension of DMFT. In order to attain an understanding of the complex physics, we approximated the VO_2 phase transition using a one-dimensional Peierls-Hubbard model that includes the key ingredients of its low-energy physics and solved it with increasingly complex treatments of electronic correlations. We identified a unique feature of electronic correlations in the Peierls-Hubbard model: the nonlocality of structural energetics is important, whereas Hubbard U only influences dimerization weakly. The results satisfactorily explain why unorthodox NSP DFT+U methods are successful. They also guide us in designing a single-particle density matrix functional (i.e. NSP DFT+U+α+β) that qualitatively and semi-quantitatively captures the structural and electronic properties of R and M_1, resolving their energy ordering. Our DFT+U+α+β predicts that neither the R nor the M_1 phase has any soft phonon modes under compressive strain, implying a first-order phase transition. Our approach successfully predicts the temperature-strain phase diagram of VO_2 within the harmonic approximation. It should be noted that this phase diagram has never been attempted from first principles until now. We now have a first-principles tool to study the phase diagram of VO_2 at finite temperatures, excluding the M_2 phase. This begins a new era of ab-initio engineering to complement massive experimental efforts, some of which are being undertaken in U.S. semiconductor

corporations. One of the remaining challenges is to include the other magnetic phases of VO_2 to expand its theoretically determined phase diagram, which would require more advanced methods such as cluster DMFT. Another important challenge is computing phonon interactions to predict other observables such as thermal conductivity.

Bibliography

[1] P. Hohenberg. Inhomogeneous Electron Gas. *Physical Review*, 136(3B):B864–B871, November 1964.

[2] W. Kohn and L. J. Sham. Self-Consistent Equations Including Exchange and Correlation Effects. *Physical Review*, 140(4A):A1133–A1138, November 1965.

[3] John P. Perdew, Kieron Burke, and Matthias Ernzerhof. Generalized gradient approximation made simple. *Phys. Rev. Lett.*, 77:3865, Oct 1996.

[4] G. Kotliar, S. Y. Savrasov, K. Haule, V. S. Oudovenko, O. Parcollet, and C. A. Marianetti. Electronic structure calculations with dynamical mean-field theory. *Rev. Mod. Phys.*, 78:865, 2006.

[5] M. W. Haverkort, Z. Hu, A. Tanaka, W. Reichelt, S. V. Streltsov, M. A. Korotin, V. I. Anisimov, H. H. Hsieh, H. J. Lin, C. T. Chen, D. I. Khomskii, and L. H. Tjeng. Orbital-assisted metal-insulator transition in vo2. *Phys. Rev. Lett.*, 95:196404, 2005.

[6] N. B. Aetukuri, A. X. Gray, M. Drouard, M. Cossale, L. Gao, A. H. Reid, R. Kukreja, H. Ohldag, C. A. Jenkins, E. Arenholz, K. P. Roche, H. A. Duerr, M. G. Samant, and S. Parkin. Control of the metal-insulator transition in vanadium dioxide by modifying orbital occupancy. *Nature Physics*, 9:661, 2013.

[7] V. Eyert. The metal-insulator transitions of vo2: a band theoretical approach. *Annalen Der Physik*, 11:650, 2002.

[8] Zhiyong Zhu and Udo Schwingenschlögl. Comprehensive picture of $\mathbf{vo_2}$ from band theory. *Phys. Rev. B*, 86:075149, 2012.

[9] Hyowon Park, Andrew J. Millis, and Chris A. Marianetti. Total energy calculations using dft+dmft: Computing the pressure phase diagram of the rare earth nickelates. *Phys. Rev. B*, 89:245133, 2014.

[10] F. J. Morin. Oxides which show a metal-to-insulator transition at the neel temperature. *Phys. Rev. Lett.*, 3:34, 1959.

[11] J. P. Pouget, H. Launois, T. M. Rice, P. Dernier, A. Gossard, G. Villeneuve, and P. Hagenmuller. Dimerization of a linear heisenberg chain in the insulating phases of $\mathrm{v}_{1-x}\mathrm{cr}_x\mathrm{o}_2$. *Phys. Rev. B*, 10:1801, Sep 1974.

[12] M. Nakano, K. Shibuya, D. Okuyama, T. Hatano, S. Ono, M. Kawasaki, Y. Iwasa, and Y. Tokura. Collective bulk carrier delocalization driven by electrostatic surface charge accumulation. *Nature*, 487:459, 2012.

[13] G. Stefanovich, A. Pergament, and D. Stefanovich. Electrical switching and mott transition in vo2. *Journal Of Physics-condensed Matter*, 12:8837, 2000.

[14] V. R. Morrison, R. P. Chatelain, K. L. Tiwari, A. Hendaoui, A. Bruhacs, M. Chaker, and B. J. Siwick. A photoinduced metal-like phase of monoclinic vo2 revealed by ultrafast electron diffraction. *Science*, 346:445, 2014.

[15] D. Wegkamp, M. Herzog, L. Xian, M. Gatti, P. Cudazzo, C. L. Mcgahan, R. E. Marvel, J. Haglund, A. Rubio, M. Wolf, and J. Staehler. Instantaneous band gap collapse in photoexcited monoclinic vo2 due to photocarrier doping. *Phys. Rev. Lett.*, 113:216401, 2014.

[16] J. M. Atkin, S. Berweger, E. K. Chavez, M. B. Raschke, J. Cao, W. Fan, and J. Wu. Strain and temperature dependence of the insulating phases of vo2 near the metal-insulator transition. *Phys. Rev. B*, 85:020101, 2012.

[17] J. H. Park, J. M. Coy, T. S. Kasirga, C. Huang, Z. Fei, S. Hunter, and D. H. Cobden. Measurement of a solid-state triple point at the metal-insulator transition in vo2. *Nature*, 500:431, 2013.

[18] C. N. Berglund and H. J. Guggenheim. Electronic properties of vo_2 near the semiconductor-metal transition. *Phys. Rev.*, 185:1022, 1969.

[19] D. B. McWhan, M. Marezio, J. P. Remeika, and P. D. Dernier. X-ray diffraction study of metallic vo_2. *Phys. Rev. B*, 10:490, 1974.

[20] Kki Takanashi, Hiroshi Yasuoka, Yutaka Ueda, and Kji Kosuge. Nmr studies of vo2 and v1-xwxo2. *Journal of the Physical Society of Japan*, 52(11):3953, 1983.

[21] J. M. Longo and K. Kierkega.p. A refinement of structure of vo2. *Acta Chemica Scandinavica*, 24:420, 1970.

[22] G. Andersson. Studies on vanadium oxides. ii. the crystal structure of vanadium dioxide. *Acta Chim. Scand.*, 10:623, 1956.

[23] Hans W. Verleur, A. S. Barker, and C. N. Berglund. Optical properties of vo_2 between 0.25 and 5 ev. *Phys. Rev.*, 172:788, Aug 1968.

[24] Larry A. Ladd and William Paul. Optical and transport properties of high quality crystals of {V2O4} near the metallic transition temperature. *Solid State Communications*, 7(4):425, 1969.

[25] A. Cavalleri, C. Toth, C. W. Siders, J. A. Squier, F. Raksi, P. Forget, and J. C. Kieffer. Femtosecond structural dynamics in vo2 during an ultrafast solid-solid phase transition. *Phys. Rev. Lett.*, 87:237401, 2001.

[26] S. Lysenko, V. Vikhnin, F. Fernandez, A. Rua, and H. Liu. Photoinduced insulator-to-metal phase transition in Vo_2 crystalline films and model of dielectric susceptibility. *Phys. Rev. B*, 75:075109, 2007.

[27] Jaewoo Jeong, Nagaphani Aetukuri, Tanja Graf, Thomas D. Schladt, Mahesh G. Samant, and Stuart S. P. Parkin. Suppression of metal-insulator transition in vo2 by electric field-induced oxygen vacancy formation. *SCIENCE*, 339:1402–1405, 2013.

[28] Yanfeng Gao, Shaobo Wang, Hongjie Luo, Lei Dai, Chuanxiang Cao, Yiliao Liu, Zhang Chen, and Minoru Kanehira. Enhanced chemical stability of vo2 nanoparticles by the formation of sio2/vo2 core/shell structures and the application to transparent and flexible vo2-based composite foils with excellent thermochromic properties for solar heat control. *Energy Environ. Sci.*, 5:6104, 2012.

[29] J. B. Goodenough. 2 components of crystallographic transition in vo2. *Journal Of Solid State Chemistry*, 3:490, 1971 OI Goodenough, John Bannister/0000-0001-9350-3034.

[30] M. M. Qazilbash, K. S. Burch, D. Whisler, D. Shrekenhamer, B. G. Chae, H. T. Kim, and D. N. Basov. Correlated metallic state of vanadium dioxide. *Phys. Rev. B*, 74:205118, Nov 2006.

[31] J. P. Pouget, H. Launois, J. P. Dhaenens, P. Merenda, and T. M. Rice. Electron localization induced by uniaxial stress in pure vo2. *Phys. Rev. Lett.*, 35:873, 1975.

[32] Hyun-Tak Kim, Byung-Gyu Chae, Doo-Hyeb Youn, Gyungock Kim, Kwang-Yong Kang, Seung-Joon Lee, Kwan Kim, and Yong-Sik Lim. Raman study of electric-field-induced first-order metal-insulator transition in vo2-based devices. *Applied Physics Letters*, 86(24):242101, 2005.

[33] A. Zylbersztejn and N. F. Mott. Metal-insulator transition in vanadium dioxide. *Phys. Rev. B*, 11:4383, 1975.

[34] M. A. Korotin, N. A. Skorikov, and V. I. Anisimov. Variation of orbital symmetry of the localized 3d(1) electron of the v4+ ion upon the metal-insulator transition in vo2. *Physics Of Metals And Metallography*, 94:17, 2002.

[35] A. Liebsch, H. Ishida, and G. Bihlmayer. Coulomb correlations and orbital polarization in the metal-insulator transition of vo2. *Phys. Rev. B*, 71:085109, 2005.

[36] V. Eyert. Vo2: A novel view from band theory. *PHYSICAL REVIEW LETTERS*, 107:016401, 2011.

[37] A. Continenza, S. Massidda, and M. Posternak. Self-energy corrections in vo2 within a model gw scheme. *Phys. Rev. B*, 60:15699, 1999.

[38] M. Gatti, F. Bruneval, V. Olevano, and L. Reining. Understanding correlations in vanadium dioxide from first principles. *Phys. Rev. Lett.*, 99:266402, 2007.

[39] Xun Yuan, Yubo Zhang, Tesfaye A. Abtew, Peihong Zhang, and Wenqing Zhang. Vo_2: Orbital competition, magnetism, and phase stability. *Phys. Rev. B*, 86:235103, 2012.

[40] F. Tran and P. Blaha. Accurate band gaps of semiconductors and insulators with a semilocal exchange-correlation potential. *Phys. Rev. Lett.*, 102:226401, 2009.

[41] S. Biermann, A. Poteryaev, A. I. Lichtenstein, and A. Georges. Dynamical singlets and correlation-assisted peierls transition in vo2. *Phys. Rev. Lett.*, 94:026404, 2005.

[42] M. S. Laad, L. Craco, and E. Mueller-hartmann. Metal-insulator transition in rutile-based vo2. *Phys. Rev. B*, 73:195120, 2006.

[43] A. S. Belozerov, M. A. Korotin, V. I. Anisimov, and A. I. Poteryaev. Monoclinic m-1 phase of vo2: mott-hubbard versus band insulator. *Phys. Rev. B*, 85:045109, 2012.

[44] W. H. Brito, M. Aguiar, K. Haule, and G. Kotliar. Metal-insulator transition in vo2: a dft + dmft perspective. *Phys. Rev. Lett.*, 117:056402, 2016.

[45] H. Park, K. Haule, and G. Kotliar. Cluster dynamical mean field theory of the mott transition. *Phys. Rev. Lett.*, 101:186403, 2008.

[46] J. M. Tomczak, F. Aryasetiawan, and S. Biermann. Effective bandstructure in the insulating phase versus strong dynamical correlations in metallic vo(2). *Phys. Rev. B*, 78:115103, 2008.

[47] T. J. Huffman, Peng Xu, M. M. Qazilbash, E. J. Walter, H. Krakauer, Jiang Wei, D. H. Cobden, H. A. Bechtel, M. C. Martin, G. L. Carr, and D. N. Basov. Anisotropic infrared response of vanadium dioxide microcrystals. *Phys. Rev. B*, 87:115121, Mar 2013.

[48] M. Cwik, T. Lorenz, J. Baier, R. Müller, G. André, F. Bourée, F. Lichtenberg, A. Freimuth, R. Schmitz, E. Müller-Hartmann, and M. Braden. Crystal and magnetic structure of latio$_3$: evidence for nondegenerate t_{2g} orbitals. *Phys. Rev. B*, 68:060401, 2003.

[49] E. Pavarini, S. Biermann, A. Poteryaev, A. I. Lichtenstein, A. Georges, and O. K. Andersen. Mott transition and suppression of orbital fluctuations in orthorhombic $3d^1$ perovskites. *Phys. Rev. Lett.*, 92:176403, Apr 2004.

[50] Hyowon Park, Andrew J. Millis, and Chris A. Marianetti. Site-selective mott transition in rare-earth-element nickelates. *Phys. Rev. Lett.*, 109:156402, 2012.

[51] V. Eyert. vo$_2$: A novel view from band theory. *Phys. Rev. Lett.*, 107:016401, 2011.

[52] S. Kim, K. Kim, C. Kang, and B. I. Min. Correlation-assisted phonon softening and the orbital-selective peierls transition in vo2. *Phys. Rev. B*, 87:195106, 2013.

[53] Ricardo Grau-Crespo, Hao Wang, and Udo Schwingenschlögl. Why the heyd-scuseria-ernzerhof hybrid functional description of vo$_2$ phases is not correct. *Phys. Rev. B*, 86:081101, 2012.

[54] Fan Zheng, Hiroyuki Takenaka, Fenggong Wang, Nathan Z. Koocher, and Andrew M. Rappe. First-Principles Calculation of the Bulk Photovoltaic Effect in CH 3 NH 3 PbI 3 and CH 3 NH 3 PbI 3 x Cl x. *The Journal of Physical Chemistry Letters*, 6(1):31–37, January 2015.

[55] R. M. Wentzcovitch, W. W. Schulz, and P. B. Allen. Vo2 - peierls or mott-hubbard - a view from band theory. *Phys. Rev. Lett.*, 72:3389, 1994.

[56] P. B. Allen, R. M. Wentzcovitch, W. W. Schulz, and P. C. Canfield. Resistivity of the high-temperature metallic phase of vo2. *Phys. Rev. B*, 48:4359, 1993.

[57] J. D. Budai, J. Hong, M. E. Manley, E. D. Specht, C. W. Li, J. Z. Tischler, D. L. Abernathy, A. H. Said, B. M. Leu, L. A. Boatner, R. J. Mcqueeney, and O. Delaire. Metallization of vanadium dioxide driven by large phonon entropy. *Nature*, 515:535, 2014.

[58] S. Xu, X. Shen, K. A. Hallman, J. Haglund, and S. T. Pantelides. Unified band-theoretic description of structural, electronic, and magnetic properties of vanadium dioxide phases. *Phys. Rev. B*, 95:125105, 2017.

[59] Du šan Plašienka, Roman Martoňák, and Marcus C. Newton. Ab initio. *Phys. Rev. B*, 96:054111, Aug 2017.

[60] G. Liu, X. Deng, and R. Wen. Electronic and optical properties of monoclinic and rutile vanadium dioxide. *Journal Of Materials Science*, 45:3270, 2010.

[61] John Maddox. Crystals from first principles. *Nature*, 335:201, 1988.

[62] S. Tsuneyuki, M. Tsukada, H. Aoki, and Y. Matsui. First-principles interatomic potential of silica applied to molecular dynamics. *Phys. Rev. Lett.*, 61:869, 1988.

[63] I. Di Marco, J. Minár, S. Chadov, M. I. Katsnelson, H. Ebert, and A. I. Lichtenstein. Correlation effects in the total energy, the bulk modulus, and the lattice constant of a transition metal: Combined local-density approximation and dynamical mean-field theory applied to ni and mn. *Phys. Rev. B*, 79:115111, Mar 2009.

[64] Geunsik Lee, Hyo Seok Ji, Yeongkwan Kim, Changyoung Kim, Kristjan Haule, Gabriel Kotliar, Bumsung Lee, Seunghyun Khim, Kee Hoon Kim, Kwang S. Kim, Ki-Seok Kim, and Ji Hoon Shim. Orbital selective fermi surface shifts and mechanism of high T_c superconductivity in correlated aFeAs (a = Li, na). *Phys. Rev. Lett.*, 109:177001, Oct 2012.

[65] Markus Aichhorn, Leonid Pourovskii, and Antoine Georges. Importance of electronic correlations for structural and magnetic properties of the iron pnictide superconductor lafeaso. *Phys. Rev. B*, 84:054529, Aug 2011.

[66] B. Amadon. A self-consistent dft + dmft scheme in the projector augmented wave method: applications to cerium, ce2o3 and pu2o3 with the hubbard i solver and comparison to dft + u. *J. Phys.: Condens. Matter*, 24:075604, 2012.

[67] C. Sommers and S. Doniach. 1st principles calculation of intra-atomic correlation energy in vo-2. *Solid State Communications*, 28:133, 1978.

[68] D. Paquet and P. Lerouxhugon. Electron correlations and electron-lattice interactions in the metal-insulator, ferroelastic transition in vo2 - a thermodynamical study. *Phys. Rev. B*, 22:5284, 1980.

[69] P. B. Littewood and V Heine. The effect of electron-electron interaction on the peierls transition in metals with strong nesting of fermi surfaces. *J. Phys. C:Solid State Phys.*, 14:2943, 1981.

[70] H. B. Pang and S. D. Liang. Density-matrix renormalization-group studies of the alternating hubbard-model. *Phys. Rev. B*, 51:10287, 1995.

[71] Antoine Georges, Gabriel Kotliar, Werner Krauth, and Marcelo J. Rozenberg. Dynamical mean-field theory of strongly correlated fermion systems and the limit of infinite dimensions. *Rev. Mod. Phys.*, 68:13, 1996.

[72] Thomas Maier, Mark Jarrell, Thomas Pruschke, and Matthias H. Hettler. Quantum cluster theories. *Rev. Mod. Phys.*, 77:1027, 2005.

[73] M. Capone, M. Civelli, S. S. Kancharla, C. Castellani, and G. Kotliar. Cluster-dynamical mean-field theory of the density-driven mott transition in the one-dimensional hubbard model. *Phys. Rev. B*, 69:195105, 2004.

[74] M. H. Hettler, A. N. Tahvildar-Zadeh, M. Jarrell, T. Pruschke, and H. R. Krishnamurthy. Nonlocal dynamical correlations of strongly interacting electron systems. *Phys. Rev. B*, 58:R7475, 1998.

[75] C. J. Bolech, S. S. Kancharla, and G. Kotliar. Cellular dynamical mean-field theory for the one-dimensional extended hubbard model. *Phys. Rev. B*, 67:075110, Feb 2003.

[76] A. Go and G. S. Jeon. Cellular dynamical mean-field study of the one-dimensional peierls hubbard model. *Journal Of The Korean Physical Society*, 56:994, 2010.

[77] U. Schollwöck. The density-matrix renormalization group. *Rev. Mod. Phys.*, 77:259, 2005.

[78] B. Bauer et al. The alps project release 2.0: open source software for strongly correlated systems. *J. Stat. Mech.*, page P05001, 2011.

[79] A.F. Albuquerque, F. Alet, P. Corboz, P. Dayal, A. Feiguin, S. Fuchs, L. Gamper, E. Gull, S. G, A. Honecker, R. Igarashi, M. Kr, A. Kozhevnikov, A. Lhli, S.R. Manmana, M. Matsumoto, I.P. McCulloch, F. Michel, R.M. Noack, G. Pawlowski, L. Pollet, T. Pruschke, U. Schollwand S. Todo, S. Trebst, M. Troyer, P. Werner, and S. Wessel. The alps project release 1.3: Open-source software for strongly correlated systems. *Journal of Magnetism and Magnetic Materials*, 310:1187, 2007. Proceedings of the 17th International Conference on Magnetism.

[80] S. Shin, S. Suga, M. Taniguchi, M. Fujisawa, H. Kanzaki, A. Fujimori, H. Daimon, Y. Ueda, K. Kosuge, and S. Kachi. Vacuum-ultraviolet reflectance and photoemission study of the metal-insulator phase transitions in vo_2, v_6o_{13}, and v_2o_3. *Phys. Rev. B*, 41:4993, 1990.

[81] G. Kresse and J. Hafner. Ab initio molecular dynamics for liquid metals. *Physical Review B*, 47(1):558561, 1993.

[82] G. Kresse and J. Hafner. Ab initio molecular-dynamics simulation of the liquid-metal amorphous-semiconductor transition in germanium. *Physical Review B*, 49(20):14251–14269, May 1994.

[83] G. Kresse and J. Furthmuller. Efficiency of ab-initio total energy calculations for metals and semiconductors using a plane-wave basis set. *Computational Materials Science*, 6(1):15, 1996.

[84] G. Kresse. Efficient iterative schemes for ab initio total-energy calculations using a plane-wave basis set. *Physical Review B*, 54(16):11169, 1996.

[85] P. E. Blöchl. Projector augmented-wave method. *Physical Review B*, 50(24):17953–17979, December 1994.

[86] G. Kresse. From ultrasoft pseudopotentials to the projector augmented-wave method. *Physical Review B*, 59(3):1758, 1999.

[87] Vladimir I Anisimov, F Aryasetiawan, and A I Lichtenstein. First-principles calculations of the electronic structure and spectra of strongly correlated systems: the LDA + U method. *Journal of Physics: Condensed Matter*, 9(4):767–808, January 1997.

[88] Hyowon Park, Andrew J. Millis, and Chris A. Marianetti. Density functional versus spin-density functional and the choice of correlated subspace in multivariable effective action theories of electronic structure. *Phys. Rev. B*, 92:035146, 2015.

[89] Hendrik J. Monkhorst and James D. Pack. Special points for Brillouin-zone integrations. *Physical Review B*, 13(12):5188–5192, June 1976.

[90] K. Parlinski, Z. Q. Li, and Y. Kawazoe. First-principles determination of the soft mode in cubic zro_2. *Phys. Rev. Lett.*, 78:4063, 1997.

[91] Koichi Momma and Fujio Izumi. VESTA : a three-dimensional visualization system for electronic and structural analysis. *Journal of Applied Crystallography*, 41(3):653–658, May 2008.

[92] K. Kosuge. Phase transition in vo2. *J. Phys. Soc. Jpn.*, 22:551, 1967.

[93] Donat J. Adams and Daniele Paseerone. Insight into structural phase transitions from the decouled anharmonic mode approximation. *J. Phys.: Condens. Matter*, 28:305401, 2016.

[94] K. Okazaki, H. Wadati, A. Fujimori, M. Onoda, Y. Muraoka, and Z. Hiroi. Photoemission study of the metal-insulator transition in vo2/tio2(001): evidence for strong electron-electron and electron-phonon interaction. *Phys. Rev. B*, 69:165104, 2004.

[95] P. F. Bongers. Anisotropy of the electrical conductivity of vo(2) single crystals. *SOLID STATE COMMUNICATIONS*, 3:275, 1965.

[96] X. Yuan, W. Zhang, and P. Zhang. Hole-lattice coupling and photoinduced insulator-metal transition in vo2. *Phys. Rev. B*, 88:035119, 2013.

[97] B. Lazarovits, K. Kim, K. Haule, and G. Kotliar. Effects of strain on the electronic structure of vo2. *Phys. Rev. B*, 81:115117, 2010.

[98] H. Terauchi and J. B. Cohen. Diffuse x-ray-scattering due to lattice instability near metal-semiconductor transition in vo2. *Phys. Rev. B*, 17:2494, 1978.

[99] J. R. Brews. Symmetry considerations and the vanadium dioxide phase transition. *Phys. Rev. B*, 1:2557, 1970.

[100] M. Marezio, D. B. McWhan, J. P. Remeika, and P. D. Dernier. Structural aspects of the metal-insulator transitions in cr-doped vo_2. *Phys. Rev. B*, 5:2541, 1972.

[101] J. Cao, Y. Gu, W. Fan, L. Q. Chen, D. F. Ogletree, K. Chen, N. Tamura, M. Kunz, C. Barrett, J. Seidel, and J. Wu. Extended mapping and exploration of the vanadium dioxide stress-temperature phase diagram. *Nano Letters*, 10:2667, 2010.

[102] J. Cao, E. Ertekin, V. Srinivasan, W. Fan, S. Huang, H. Zheng, J. Yim, D. R. Khanal, D. F. Ogletree, J. C. Grossmanan, and J. Wu. Strain engineering and one-dimensional organization of metal-insulator domains in single-crystal vanadium dioxide beams. *Nature Nanotechnology*, 4:732, 2009.

[103] A. van de Walle and G. Ceder. The effect of lattice vibrations on substitutional alloy thermodynamics. *Rev. Mod. Phys.*, 74:11, 2002.

Appendix : CIX for Continous-Time Quantum Monte Carlo

In order to solve the Peierls-Hubbard model via the cluster extension of dynamical mean field theory, a cix file for cluster impurity (i.e. an isolated Hubbard dimer) should be generated to perform CT-QMC calculations.

$$\hat{H} = -t\sum_{\sigma}(\hat{c}^{\dagger}_{\sigma a}\hat{c}_{\sigma b} + \hat{c}^{\dagger}_{\sigma b}\hat{c}_{\sigma a}) + U(\hat{n}_{\uparrow a}\hat{n}_{\downarrow a} + \hat{n}_{\uparrow b}\hat{n}_{\downarrow b})$$

We will first analyze this in the usual direct basis. Let us first define the Hilbert spaces:

$N=0:$	$\|0\rangle$					
$N=1:$	$\|a_{\uparrow}\rangle$	$\|a_{\downarrow}\rangle$	$\|b_{\uparrow}\rangle$	$\|b_{\downarrow}\rangle$		
$N=2:$	$\|a_{\uparrow}a_{\downarrow}\rangle$	$\|b_{\uparrow}b_{\downarrow}\rangle$	$\|a_{\uparrow}b_{\downarrow}\rangle$	$\|a_{\downarrow}b_{\uparrow}\rangle$	$\|a_{\uparrow}b_{\uparrow}\rangle$	$\|a_{\downarrow}b_{\downarrow}\rangle$
$N=3:$	$\|a_{\downarrow}b_{\uparrow}b_{\downarrow}\rangle$	$\|a_{\uparrow}b_{\uparrow}b_{\downarrow}\rangle$	$\|a_{\uparrow}a_{\downarrow}b_{\downarrow}\rangle$	$\|a_{\uparrow}a_{\downarrow}b_{\uparrow}\rangle$		
$N=4:$	$\|a_{\uparrow}a_{\downarrow}b_{\uparrow}b_{\downarrow}\rangle$					

Let us now make the Hamiltonian matrix in each separate Hilbert space, with the ordering as given above:

$$\hat{H}_{N=0} = [0] \qquad \hat{H}_{N=1} = \begin{bmatrix} 0 & 0 & -t & 0 \\ 0 & 0 & 0 & -t \\ -t & 0 & 0 & 0 \\ 0 & -t & 0 & 0 \end{bmatrix} \qquad \hat{H}_{N=2} = \begin{bmatrix} U & 0 & -t & t & 0 & 0 \\ 0 & U & -t & t & 0 & 0 \\ -t & -t & 0 & 0 & 0 & 0 \\ t & t & 0 & 0 & 0 & 0 \\ 0 & 0 & 0 & 0 & 0 & 0 \\ 0 & 0 & 0 & 0 & 0 & 0 \end{bmatrix}$$

$$\hat{H}_{N=3} = \begin{bmatrix} U & 0 & t & 0 \\ 0 & U & 0 & t \\ t & 0 & U & 0 \\ 0 & t & 0 & U \end{bmatrix} \qquad \hat{H}_{N=4} = [2U]$$

In order to efficiently exploit CTQMC, we need to symmetrize a basis set with respect to the mirror. The irreps of the mirror are A and B.

	$00A0$					
$N=0:$	$\|0\rangle$					
	$1\uparrow A0$	$1\uparrow B0$	$1\downarrow A0$	$1\downarrow B0$		
$N=1:$	$\frac{1}{\sqrt{2}}(\|a_\uparrow\rangle + \|b_\uparrow\rangle)$	$\frac{1}{\sqrt{2}}(\|a_\uparrow\rangle - \|b_\uparrow\rangle)$	$\frac{1}{\sqrt{2}}(\|a_\downarrow\rangle + \|b_\downarrow\rangle)$	$\frac{1}{\sqrt{2}}(\|a_\downarrow\rangle - \|b_\downarrow\rangle)$		
	$20A0$	$20B0$	$20B1$	$20A1$	$2\uparrow_2 B0$	$2\downarrow_2 B$
$N=2:$	$\frac{1}{\sqrt{2}}(\|a_\uparrow a_\downarrow\rangle + \|b_\uparrow b_\downarrow\rangle)$	$\frac{1}{\sqrt{2}}(\|a_\uparrow a_\downarrow\rangle - \|b_\uparrow b_\downarrow\rangle)$	$\frac{1}{\sqrt{2}}(\|a_\uparrow b_\downarrow\rangle + \|a_\downarrow b_\uparrow\rangle)$	$\frac{1}{\sqrt{2}}(\|a_\uparrow b_\downarrow\rangle - \|a_\downarrow b_\uparrow\rangle)$	$\|a_\uparrow b_\uparrow\rangle$	$\|a_\downarrow b_\downarrow\rangle$
	$3\uparrow A0$	$3\uparrow B0$	$3\downarrow A0$	$3\downarrow B0$		
$N=3:$	$\frac{1}{\sqrt{2}}(\|a_\uparrow b_\uparrow b_\downarrow\rangle + \|a_\uparrow a_\downarrow b_\uparrow\rangle)$	$\frac{1}{\sqrt{2}}(\|a_\uparrow a_\downarrow b_\uparrow\rangle - \|a_\uparrow b_\uparrow b_\downarrow\rangle)$	$\frac{1}{\sqrt{2}}(\|a_\downarrow b_\uparrow b_\downarrow\rangle + \|a_\uparrow a_\downarrow b_\downarrow\rangle)$	$\frac{1}{\sqrt{2}}(\|a_\uparrow a_\downarrow b_\downarrow\rangle - \|a_\downarrow b_\uparrow b_\downarrow\rangle)$		
	$40A0$					
$N=4:$	$\|a_\uparrow a_\downarrow b_\uparrow b_\downarrow\rangle$					

Let us now make the Hamiltonian matrix in the symmetrized basis with respect to the mirror, with the ordering as given above:

$$\hat{H}_{N=0} = [0] \qquad \hat{H}_{N=1} = \begin{bmatrix} -t & 0 & 0 & 0 \\ 0 & t & 0 & 0 \\ 0 & 0 & -t & 0 \\ 0 & 0 & 0 & t \end{bmatrix} \qquad \hat{H}_{N=2} = \begin{bmatrix} U & 0 & 0 & -2t & 0 & 0 \\ 0 & U & 0 & 0 & 0 & 0 \\ 0 & 0 & 0 & 0 & 0 & 0 \\ -2t & 0 & 0 & 0 & 0 & 0 \\ 0 & 0 & 0 & 0 & 0 & 0 \\ 0 & 0 & 0 & 0 & 0 & 0 \end{bmatrix}$$

$$\hat{H}_{N=3} = \begin{bmatrix} U+t & 0 & 0 & 0 \\ 0 & U-t & 0 & 0 \\ 0 & 0 & U+t & 0 \\ 0 & 0 & 0 & U-t \end{bmatrix} \qquad \hat{H}_{N=4} = [2U]$$

We will now introduce a notation to classify all states, using N, S_z, irrep of point group (i.e. A or B for the dimer), and number of times point group irrep appears.

$$|NS_z\mathrm{Ir}\rangle \qquad |00A0\rangle = |0\rangle \qquad |40A0\rangle = |a_\uparrow a_\downarrow b_\uparrow b_\downarrow\rangle$$

We now need to define the symmetrized field operators.

$$\hat{c}_{A\sigma} = \frac{1}{\sqrt{2}}\left(\hat{c}_{a\sigma} + \hat{c}_{b\sigma}\right) \qquad \hat{c}_{B\sigma} = \frac{1}{\sqrt{2}}\left(\hat{c}_{a\sigma} - \hat{c}_{b\sigma}\right)$$

We need to figure how the symmetrized creation operators map one state to another.

$$\hat{c}^\dagger_{A\uparrow}|00A0\rangle = |1\uparrow A0\rangle$$
$$\hat{c}^\dagger_{A\downarrow}|00A0\rangle = |1\downarrow A0\rangle$$
$$\hat{c}^\dagger_{B\uparrow}|00A0\rangle = |1\uparrow B0\rangle$$
$$\hat{c}^\dagger_{B\downarrow}|00A0\rangle = |1\downarrow B0\rangle$$
$$\hat{c}^\dagger_{A\uparrow}|1\uparrow A0\rangle = 0$$
$$\hat{c}^\dagger_{A\downarrow}|1\uparrow A0\rangle = -\frac{1}{\sqrt{2}}(|20A0\rangle + |20A1\rangle)$$
$$\hat{c}^\dagger_{B\uparrow}|1\uparrow A0\rangle = |2\uparrow_2 B0\rangle$$
$$\hat{c}^\dagger_{B\downarrow}|1\uparrow A0\rangle = -\frac{1}{\sqrt{2}}(|20B0\rangle - |20B1\rangle)$$
$$\hat{c}^\dagger_{A\uparrow}|1\uparrow B0\rangle = -|2\uparrow_2 B0\rangle$$
$$\hat{c}^\dagger_{A\downarrow}|1\uparrow B0\rangle = -\frac{1}{\sqrt{2}}(|20B0\rangle + |20B1\rangle)$$
$$\hat{c}^\dagger_{B\uparrow}|1\uparrow B0\rangle = 0$$
$$\hat{c}^\dagger_{B\downarrow}|1\uparrow B0\rangle = -\frac{1}{\sqrt{2}}(|20A0\rangle - |20A1\rangle)$$
$$\hat{c}^\dagger_{A\uparrow}|1\downarrow A0\rangle = \frac{1}{\sqrt{2}}(|20A0\rangle + |20A1\rangle)$$
$$\hat{c}^\dagger_{A\downarrow}|1\downarrow A0\rangle = 0$$
$$\hat{c}^\dagger_{B\uparrow}|1\downarrow A0\rangle = \frac{1}{\sqrt{2}}(|20B0\rangle + |20B1\rangle)$$
$$\hat{c}^\dagger_{B\downarrow}|1\downarrow A0\rangle = |2\downarrow_2 B0\rangle$$
$$\hat{c}^\dagger_{A\uparrow}|1\downarrow B0\rangle = \frac{1}{\sqrt{2}}(|20B0\rangle - |20B1\rangle)$$
$$\hat{c}^\dagger_{A\downarrow}|1\downarrow B0\rangle = -|2\downarrow_2 B0\rangle$$
$$\hat{c}^\dagger_{B\uparrow}|1\downarrow B0\rangle = \frac{1}{\sqrt{2}}(|20A0\rangle - |20A1\rangle)$$
$$\hat{c}^\dagger_{B\downarrow}|1\downarrow B0\rangle = 0$$

$$\hat{c}^{\dagger}_{A\uparrow}|20B0\rangle = \frac{1}{\sqrt{2}}|3\uparrow B0\rangle$$
$$\hat{c}^{\dagger}_{A\downarrow}|20B0\rangle = \frac{1}{\sqrt{2}}|3\downarrow B0\rangle$$
$$\hat{c}^{\dagger}_{B\uparrow}|20B0\rangle = \frac{-1}{\sqrt{2}}|3\uparrow A0\rangle$$
$$\hat{c}^{\dagger}_{B\downarrow}|20B0\rangle = \frac{-1}{\sqrt{2}}|3\downarrow A0\rangle$$
$$\hat{c}^{\dagger}_{A\uparrow}|20B1\rangle = \frac{1}{\sqrt{2}}|3\uparrow B0\rangle$$
$$\hat{c}^{\dagger}_{A\downarrow}|20B1\rangle = \frac{-1}{\sqrt{2}}|3\downarrow B0\rangle$$
$$\hat{c}^{\dagger}_{B\uparrow}|20B1\rangle = \frac{1}{\sqrt{2}}|3\uparrow A0\rangle$$
$$\hat{c}^{\dagger}_{B\downarrow}|20B1\rangle = \frac{-1}{\sqrt{2}}|3\downarrow A0\rangle$$
$$\hat{c}^{\dagger}_{A\uparrow}|20A0\rangle = \frac{1}{\sqrt{2}}|3\uparrow A0\rangle$$
$$\hat{c}^{\dagger}_{A\downarrow}|20A0\rangle = \frac{1}{\sqrt{2}}|3\downarrow A0\rangle$$
$$\hat{c}^{\dagger}_{B\uparrow}|20A0\rangle = \frac{-1}{\sqrt{2}}|3\uparrow B0\rangle$$
$$\hat{c}^{\dagger}_{B\downarrow}|20A0\rangle = \frac{-1}{\sqrt{2}}|3\downarrow B0\rangle$$
$$\hat{c}^{\dagger}_{A\uparrow}|20A1\rangle = \frac{-1}{\sqrt{2}}|3\uparrow A0\rangle$$
$$\hat{c}^{\dagger}_{A\downarrow}|20A1\rangle = \frac{-1}{\sqrt{2}}|3\downarrow A0\rangle$$
$$\hat{c}^{\dagger}_{B\uparrow}|20A1\rangle = \frac{-1}{\sqrt{2}}|3\uparrow B0\rangle$$
$$\hat{c}^{\dagger}_{B\downarrow}|20A1\rangle = \frac{-1}{\sqrt{2}}|3\downarrow B0\rangle$$
$$\hat{c}^{\dagger}_{A\uparrow}|2\uparrow_2 B0\rangle = 0$$
$$\hat{c}^{\dagger}_{A\downarrow}|2\uparrow_2 B0\rangle = -|3\uparrow B0\rangle$$
$$\hat{c}^{\dagger}_{B\uparrow}|2\uparrow_2 B0\rangle = 0$$
$$\hat{c}^{\dagger}_{B\downarrow}|2\uparrow_2 B0\rangle = -|3\uparrow A0\rangle$$

$$\hat{c}^{\dagger}_{A\uparrow}|2\downarrow_2 B0\rangle = |3\downarrow B0\rangle$$
$$\hat{c}^{\dagger}_{A\downarrow}|2\downarrow_2 B0\rangle = 0$$
$$\hat{c}^{\dagger}_{B\uparrow}|2\downarrow_2 B0\rangle = |3\downarrow A0\rangle$$
$$\hat{c}^{\dagger}_{B\downarrow}|2\downarrow_2 B0\rangle = 0$$
$$\hat{c}^{\dagger}_{A\uparrow}|3\uparrow A0\rangle = 0$$
$$\hat{c}^{\dagger}_{A\downarrow}|3\uparrow A0\rangle = -|40A0\rangle$$
$$\hat{c}^{\dagger}_{B\uparrow}|3\uparrow A0\rangle = 0$$
$$\hat{c}^{\dagger}_{B\downarrow}|3\uparrow A0\rangle = 0$$
$$\hat{c}^{\dagger}_{A\uparrow}|3\uparrow B0\rangle = 0$$
$$\hat{c}^{\dagger}_{A\downarrow}|3\uparrow B0\rangle = 0$$
$$\hat{c}^{\dagger}_{B\uparrow}|3\uparrow B0\rangle = 0$$
$$\hat{c}^{\dagger}_{B\downarrow}|3\uparrow B0\rangle = |40A0\rangle$$
$$\hat{c}^{\dagger}_{A\uparrow}|3\downarrow A0\rangle = |40A0\rangle$$
$$\hat{c}^{\dagger}_{A\downarrow}|3\downarrow A0\rangle = 0$$
$$\hat{c}^{\dagger}_{B\uparrow}|3\downarrow A0\rangle = 0$$
$$\hat{c}^{\dagger}_{B\downarrow}|3\downarrow A0\rangle = 0$$
$$\hat{c}^{\dagger}_{A\uparrow}|3\downarrow B0\rangle = 0$$
$$\hat{c}^{\dagger}_{A\downarrow}|3\downarrow B0\rangle = 0$$
$$\hat{c}^{\dagger}_{B\uparrow}|3\downarrow B0\rangle = -|40A0\rangle$$
$$\hat{c}^{\dagger}_{B\downarrow}|3\downarrow B0\rangle = 0$$
$$\hat{c}^{\dagger}_{A\uparrow}|40A0\rangle = 0$$
$$\hat{c}^{\dagger}_{A\downarrow}|40A0\rangle = 0$$
$$\hat{c}^{\dagger}_{B\uparrow}|40A0\rangle = 0$$
$$\hat{c}^{\dagger}_{B\downarrow}|40A0\rangle = 0$$

Then, we will list the eigenvalues and eigenstates of the two-site hamiltonian.

	$c_1 = \frac{\varepsilon_-}{2t}$	$c_2 = \frac{\varepsilon_+}{2t}$
Numbering	*Energy*	*States*
1	0	$\|00A0\rangle$
2	$-t$	$\|1\uparrow A0\rangle$
3	t	$\|1\uparrow B0\rangle$
4	$-t$	$\|1\downarrow A0\rangle$
5	t	$\|1\downarrow B0\rangle$
6	0	$\|20B1\rangle$
6	U	$\|20B0\rangle$
7	$\varepsilon_- = \frac{1}{2}(U - \sqrt{16t^2 + U^2})$	$\frac{1}{c_{1,norm}}(-c_1\|20A0\rangle + \|20A1\rangle)$
7	$\varepsilon_+ = \frac{1}{2}(U + \sqrt{16t^2 + U^2})$	$\frac{1}{c_{2,norm}}(-c_2\|20A0\rangle + \|20A1\rangle)$
8	0	$\|2\uparrow_2 B0\rangle$
9	0	$\|2\downarrow_2 B0\rangle$
10	$U + t$	$\|3\uparrow A0\rangle$
11	$U - t$	$\|3\uparrow B0\rangle$
12	$U + t$	$\|3\downarrow A0\rangle$
13	$U - t$	$\|3\downarrow B0\rangle$
14	$2U$	$\|40A0\rangle$

```
# Cix file for cluster DMFT with CTQMC
# cluster_size, number of states, number of baths, maximum_matrix_size
2 14 4 2
# baths, dimension, symmetry, global flip
0          1          0    0
1          1          0    1
2          1          1    2
3          1          1    3
# cluster energies for baths, eps[k]
-1 1
#    N   K     Sz  size         tran_elm              diag_E_atom            S
1    0   0      0   1       2       4      3      5     0       0
2    1   0    0.5   1       0       7      8      6     -1.0       0.5
3    1   1    0.5   1       8       6      0      7     1.0       0.5
4    1   0   -0.5   1       7       0      6      9     -1.0       0.5
5    1   1   -0.5   1       6       9      7      0     1.0       0.5
6    2   1      0   2      11      13     10     12     0       0.0    1   1
7    2   0      0   2      10      12     11     13     -2.0       2.0    1   1
8    2   1      1   1       0      11      0     10     0       1
9    2   1     -1   1      13       0     12      0     0       1
10   3   0    0.5   1       0      14      0      0     1.0       0.5
11   3   1    0.5   1       0       0      0     14     -1.0       0.5
12   3   0   -0.5   1      14       0      0      0     1.0       0.5
13   3   1   -0.5   1       0       0     14      0     -1.0       0.5
14   4   0      0   1       0       0      0      0     0.0       0
```

```
# matrix elements
1     2   1  1  1
1     4   1  1  1
1     3   1  1  1
1     5   1  1  1
2     0   0  0
2     7   1  2  -1.0 0.0
2     8   1  1  1
2     6   1  2  0.70710678118654757 -0.70710678118654757
3     8   1  1 -1
3     6   1  2 -0.70710678118654757 -0.70710678118654757
3     0   0  0
3     7   1  2 0.0 1.0
4     7   1  2  1.0 0.0
4     0   0  0
4     6   1  2  0.70710678118654757 0.70710678118654757
4     9   1  1  1
5     6   1  2 -0.70710678118654757 0.70710678118654757
5     9   1  1 -1
5     7   1  2 0.0 -1.0
5     0   0  0
6    11   2  1 0.70710678118654757 0.70710678118654757
6    13   2  1 -0.70710678118654757 0.70710678118654757
6    10   2  1 0.70710678118654757 -0.70710678118654757
6    12   2  1 -0.70710678118654757 -0.70710678118654757
7    10   2  1 0.0 -1.0
7    12   2  1 0.0 -1.0
7    11   2  1 -1.0 0.0
7    13   2  1 -1.0 0.0
```

```
8     0   0  0
8    11   1  1 -1
8     0   0  0
8    10   1  1 -1
9    13   1  1 1
9     0   0  0
9    12   1  1 1
9     0   0  0
10    0   0  0
10   14   1  1 -1
10    0   0  0
10    0   0  0
11    0   0  0
11    0   0  0
11    0   0  0
11   14   1  1 1
12   14   1  1 1
12    0   0  0
12    0   0  0
12    0   0  0
13    0   0  0
13    0   0  0
13   14   1  1 -1
13    0   0  0
14    0   0  0
14    0   0  0
14    0   0  0
14    0   0  0
```